Calibration of Crystal Orientation and Pattern Center of EBSD using Integrated Digital Image Correlation

Qiwei Shi, Dominique Loisnard, Chengyi Dan, Fengguo Zhang, Hongru Zhong, Han Li, Yuda Li, Zhe Chen, Haowei Wang, Stéphane Roux

Calibration of Crystal Orientation and Pattern Center of EBSD using Integrated Digital Image Correlation

Qiwei Shi[1,2], Dominique Loisnard[3], Chengyi Dan[1], Fengguo Zhang[1*], Hongru Zhong[1], Han Li[2], Yuda Li[2], Zhe Chen[1*], Haowei Wang[1], Stéphane Roux[4]

1: School of Materials Science and Engineering,
Shanghai Jiao Tong University, Shanghai, 200240, China

2: SJTU-ParisTech Elite Institute of Technology,
Shanghai Jiao Tong University, Shanghai, 200240, China

3: EdF R&D, Site des Renardières,avenue des Renardières,
Ecuelles, F-77818 Moret-sur-Loing, France

4: Université Paris-Saclay, ENS Paris-Saclay, CNRS,
LMT - Laboratoire de Mécanique et Technologie, F-91190, Gif-sur-Yvette, France

Received: date / Accepted: date

Abstract

The accuracy of electron backscatter diffraction indexation has long been limited by pattern center determination, and numerous hardware and software methods have been proposed to improve the calibration. Here, an *Integrated* Digital Image Correlation (IDIC) procedure is proposed to determine simultaneously crystal orientation and pattern center by registering experimental and simulated electron diffraction patterns. To assess the performance and robustness of the procedure, numerous case studies are reported. Noise sensitivity is first explored on virtual data to assess convergence conditions and result uncertainty up to high noise level and small detector size. Two experimental data sets are further exploited. First, a high-definition detector shows that crystal orientation uncertainty as low as 3×10^{-2} degrees can be achieved, that is at least 80% less than commercial Hough-transformation based indexation method. Different sample tilt angles are tested, IDIC indexation proves much more tolerant with imprecise tilt angles than common EBSD indexation methods. Second, fast EBSD acquisitions with a coarse definition performed during an in-situ tensile test are analyzed. A quantification of the residual noise allows one to formulate an optimized IDIC functional with a proper pixel-wise weight. With the latter refinement a two-pass procedure leads to a much enhanced precision of the determination of crystal orientation, giving access to more precise evaluation of maps of geometrically necessary dislocation densities.

Keyword: EBSD calibration, High-angular-resolution EBSD, Integrated digital image correlation, Geometrically necessary dislocations, Intragranular Substructures.

1 Introduction

Crystallographic orientation information is of vital importance in many domains of application such as materials science, geology or semi-conductor industry. Different methods have been proposed to obtain crystal orientation, such as optical reflection method [1] and chemical corrosion method [2]. In recent decades, Electron BackScatter Diffraction (EBSD) technique has revealed to be a technique of choice to obtain crystallographic orientation fields in scanning electron microscopes. This technique aims principally at obtaining orientation maps from the analysis of the Kikuchi diffraction pattern (thereafter denoted as EBSP for Electron BackScatter Pattern) by Hough-transformation or the newly emerged convolutional neural network [3, 4]. Standard EBSD usually provides results with an angular resolution of about 0.5°. Note that the definition of angular resolution is not unique in the EBSD community, and the definition adopted herein is the one given in Ref. [5], which is the uncertainty of indexed Euler angles for a sample of unique crystal orientation. This relatively high level of uncertainty has been shown [6, 5] to be mainly due to several factors:

- the specific algorithm (based on the Hough transform) used for data processing,
- a poor accuracy of positioning the Projection Center (PC)
- and the adjustment of an undeformed lattice cell.

Such an uncertainty is sufficient to evaluate local orientation maps but cannot reveal elastic strains, which are associated with low deformations of diffraction images. The accuracy of crystal rotation measurement by *quaternion correlation* on a series of EBSD images is also limited by crystallographic indexing [7].

High-(angular) Resolution EBSD (HR-EBSD) — exploiting high-definition EBSPs registered onto a reference one through Digital Image Correlation (DIC) — has been proposed to obtain *relative* crystallographic orientations with a much higher accuracy [8, 9]. It has been shown that HR-EBSD enables the elastic strains to be measured with acceptable uncertainties and excellent spatial resolution [10]. Both *local* DIC algorithm based on cross-correlation [8] and *(integrated) global* DIC framework [11, 12, 13, 14] have been adopted in HR-EBSD. The latter method proves fast and precise for both simulated and experimental EBSPs. Global DIC can also measure grain-level absolute stress without simulated reference EBSP [15]. Yet, for both algorithms, the final results of HR-EBSD are limited by the accuracy of the projection parameters [16, 13]. Other advanced EBSD analyses, such as tetragonality mapping of martensite [17], also require precise PC values.

Knowing the crucial role of the EBSD calibration parameters in the determination of elastic strains, many groups studying HR-EBSD have contributed to the improvement of calibration. The different envisaged strategies can be cast into two groups: *hardware* and *software* based methods. The former ones imply the recourse to specific devices during acquisition, such as a "nose-cone" casting shadow on EBSP detector [18], a mobile screen [19, 20], or a strain-free reference crystal placed near the sample [21]. As pointed out by Pang *et al.* [22], these *hardware* methods suffer from drawbacks like prolonged acquisition time, inconsistent camera position, loss of information due to shadowing and difficulty to reposition the sample height accurately after even a slight motion. Nonetheless, as hardware methods provide independent calibrations, they constitute a highly valuable basis for comparison with software methods.

Software-based EBSD calibrations — and their accompanying full EBSP matching Euler angle refinement —

have undergone rapid developments in recent years. The basic idea is to tune the projection parameters (and in particular the three coordinates of the PC) in order to maximize the similarity between experimental and *simulated* EBSPs. Both *kinematic* and *dynamical* EBSP simulations have been used to generate the computed EBSPs [23], and the latter methodology was observed to provide a higher similarity with experimental pattern and thus better calibration precision. Two softwares are available for dynamical EBSP simulations, namely EMsoft [24] and ESPRIT DynamicS from Bruker Nano GmbH. To achieve the optimization of the projection parameters, many algorithms have been suggested, such as a Nelder-Mead algorithm [25, 26, 22], evolution algorithm [27], SNOBFIT algorithm [22], as well as non-disclosed ones used in commercial software [28]. The PC calibration uncertainty has been shown to reach values as low as 10^{-5} times the pattern width for virtual EBSPs and 5×10^{-4} for experimental ones. The reported Euler angles uncertainty is also very low: 0.03° for a 640×480 pixel EBSP used for the analysis of a tungsten carbide sample [29]. A comparable, though slightly higher uncertainty estimation was reported for a 1600×1200 pixel EBSP of silicon crystals [28].

Different regularization strategies on PC values to improve calibration accuracy have been proposed in recent years, such as the affine and projective PC values adopted by Winkelmann *et al.* [30]. Refined geometry model of PC values indeed improved the calibration. Pang *et al.* [22] considered several neighbouring EBSPs altogether in a "global" optimization, thus resulting in enhanced robustness and lower uncertainties in PC values at the expense of a higher computing cost of the process. Moreover, the assumption that the PCs of a cluster of pixels obey a postulated geometric regularity may not hold, as for samples having a rough surface. In the following, a two-step procedure is proposed: after a first determination of PC for each pixel without a priori assumptions, one may judge whether a geometric regularity is legitimate, and, if so, filter the data to enforce this regularity.

The present work relies on an IDIC framework for calibrating EBSD, including refinement of both Euler angles and PC position. Although IDIC has already been used for EBSD, its use, with simulated patterns, to calibrate the pattern center and Euler angles, is the novelty of the present paper. It is shown to lead to very precise and robust determinations in particular when compared to commercial codes. Section 2 introduces the chosen notations, and briefly recalls the principle of EBSP generation, including the projection parameters. Then, the IDIC data processing method for EBSD calibration is detailed. Section 3 reports the performance of the algorithm on virtual (numerically generated) EBSPs with different noise levels and different EBSP sizes. Section 4 shows the algorithm performance on high-resolution EBSPs of a polycrystalline Al alloy. Section 5 showcases the polycrystal Al alloy subjected to in-situ tensile test with conventional high-speed EBSD acquisition conditions. These examples show that the specific implementation of the IDIC method proposed herein turns out to be more robust and much faster than previously proposed calibration techniques, and more precise than current indexation methods.

2 Integrated DIC for EBSD calibration

An alternative to cross-correlation of Zones of Interest (ZOIs) (also known as *local* DIC) has been proposed as *global* DIC [31, 32]. The global approach uses the entire region of interest, once and only once, thus offering a simple handling of noise sensitivity, in contrast with many overlapping ZOIs for local DIC which naturally induce uneven weighting of EBSP pixels and build intricate correlations. Besides, global DIC provides a residual field, which is

calculated at each pixel and constitutes a reliable and robust way for characterizing registration errors. Additional information is also present in the residual field, as will be illustrated in Section 5.

Integrated Digital Image Correlation (IDIC) has been introduced to measure *directly* and *optimally* the geometric transformation of interest (or parameters quantifying it) from image registrations. This framework allows one to use a set of kinematic fields dedicated to the problem at hand [33, 34, 35]. The measured displacement fields are expressed within a "kinematic basis" that is tailored *a priori* to the studied physical phenomena (and potentially including the artefacts of image formation and acquisition). No additional degrees of freedom are allowed in the displacement field. This technique can be adapted to EBSD calibration analyses since the electron diffraction geometry can be incorporated in the kinematic basis through a few projection parameters. The positioning of query points on master pattern through experimental geometry of EBSD has been detailed by several previous works, such as the Lambert projection formula [36] and the spherical projection [37]. Thus, an IDIC-based algorithm has been developed to calibrate EBSD tests and is detailed in this section. The projection geometry of EBSP is recalled in figure 1 together with the reference system used in the paper.

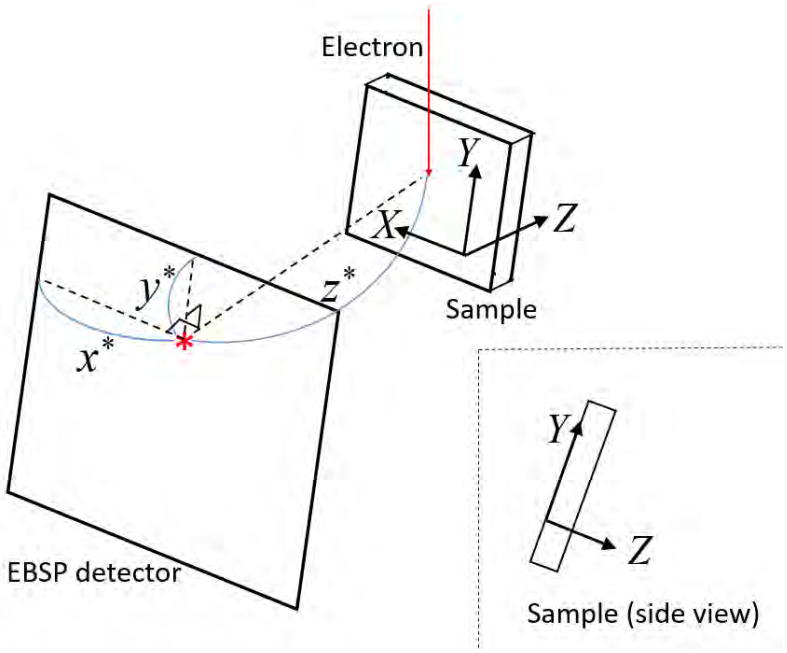

Figure 1: Coordinate systems (x, y, z) associated to EBSP detector and (X, Y, Z) associated to sample

2.1 Algorithm

The hereby proposed algorithm is based on the assumption that only 6 projection parameters (namely, the three coordinates of the projection center $\boldsymbol{x}^* = (x^*,\ y^*,\ z^*)$ and the three Euler angles $(\varphi_1, \phi, \varphi_2)$ of the crystal orientations basically determine an EBSP for a given crystal. The effect of elastic/plastic strains on EBSP is not considered for the present study, as for conventional EBSD, although their effects on calibration results will be readily visible. Several works have been devoted to measuring PC values *and* elastic strains by HR-EBSD recently. Alkorta made it clear through projection formula that HR-EBSD cannot identify both PC value and elastic strain simultaneously, as different parameters could lead to non-distinguishable EBSPs [38]. Later, Alkorta *et al.* employed the projection

formula and plane stress hypothesis to calibrate PC values [39], but the performance of the technique is limited by sample tilt error, sample surface roughness and misorientation between HR-EBSD acquisition points. Fullwood *et al.* [40] employes simulated EBSP to estimate PC coordinates and elastic strains of experimental EBSPs, by minimizing strains on known traction-free EBSPs. Though absolute yet less precise strain levels are obtained in this way, the method needs to be tested on samples without known stress-free points. Vermeij *et al.* [15] proposes to calibrate one set of PC values for the entire HR-EBSD acquisition along with plane stress hypothesis, yet the technique has not been tested on experimental dataset as the degrees of freedom becomes prohibitively large and challenges computing robustness. As a result, it is chosen in the present study to neglect the elastic strain and focus on PC and crystal orientations to fully accommodate the EBSD geometry, including sample tilt angle and surface roughness. Addressing the estimation of elastic strain is deferred to future works. The projection center is assumed to be a singular point although Monte Carlo simulations show that the backscatter electrons are emitted from a region of 200-300 nm extension [41], which is negligible in front of the EBSP pixel size (mostly larger than 20 µm). It should be noted that all the corrections of projection parameter variations summed up in [13], such as beam-induced shift and sample inclination correction, are no longer needed here, as their impacts are intrinsically included in the proposed algorithm. The SEM distortions and background are secondary effects and thus not considered in the current paper. Modern EBSD systems can remove automatically static background, thus provide balanced gray levels and well contrasted EBSPs. The hereby proposed algorithm takes these EBSPs as input images.

The EBSP screen is chosen as the reference defining the (x, y) plane, or $z = 0$. The unit vector $\boldsymbol{w}$ linking the pattern center to each pixel $\boldsymbol{x} = (x, y, z = 0)$ of the screen can be expressed as

$$\boldsymbol{w} = \frac{(\boldsymbol{x} - \boldsymbol{x}^*)}{|\boldsymbol{x} - \boldsymbol{x}^*|} \tag{1}$$

In order to rotate this vector from the screen frame of reference $\boldsymbol{w}$ to that of the spherical master pattern, $\boldsymbol{v}$, one should multiply it by a rotation operator $\boldsymbol{Q}$

$$\boldsymbol{v} = \boldsymbol{Q}\boldsymbol{w} \tag{2}$$

whose expression, using the Euler angles, reads in Bunge notations:

$$\boldsymbol{Q} = \begin{bmatrix} \cos\varphi_1 \cos\varphi_2 - \sin\varphi_1 \sin\varphi_2 \cos\phi & \sin\varphi_1 \cos\varphi_2 + \cos\varphi_1 \sin\varphi_2 \cos\phi & \sin\varphi_2 \sin\phi \\ -\cos\varphi_1 \sin\varphi_2 - \sin\varphi_1 \cos\varphi_2 \cos\phi & -\sin\varphi_1 \sin\varphi_2 + \cos\varphi_1 \cos\varphi_2 \cos\phi & \cos\varphi_2 \sin\phi \\ \sin\varphi_1 \sin\phi & -\cos\varphi_1 \sin\phi & \cos\phi \end{bmatrix} \tag{3}$$

EMsoft generates a master pattern by dynamical simulation, which is originally defined on the surface of a sphere centered on the interaction volume, and has to be projected onto a 2D plane to generate EBSPs of any crystal orientation. Several projection methods have been considered in the EBSD simulation community, such as spherical or Lambert projections. The spherical projection, as illustrated in Figure 2a, is adopted herein where the surface of the unit sphere is projected onto the equatorial plane from the north pole, denoted $\boldsymbol{n} = (0, 0, 1)^\top$. The projection of $\boldsymbol{v}$ onto this master pattern plane, $\boldsymbol{u}$, is written

$$\boldsymbol{u} = \frac{\boldsymbol{n} - \boldsymbol{v}}{(1 - \boldsymbol{v}.\boldsymbol{n})} - \boldsymbol{n} \tag{4}$$

Thus the projected position, $\boldsymbol{u}(\boldsymbol{x})$, on the master pattern can be expressed explicitly as a function of $\boldsymbol{x}$ and of the

projection parameters $(\varphi_1, \phi, \varphi_2, x^*, y^*, z^*)$. The expression is quite lengthy but presents no difficulty, and is thus not displayed explicitly.

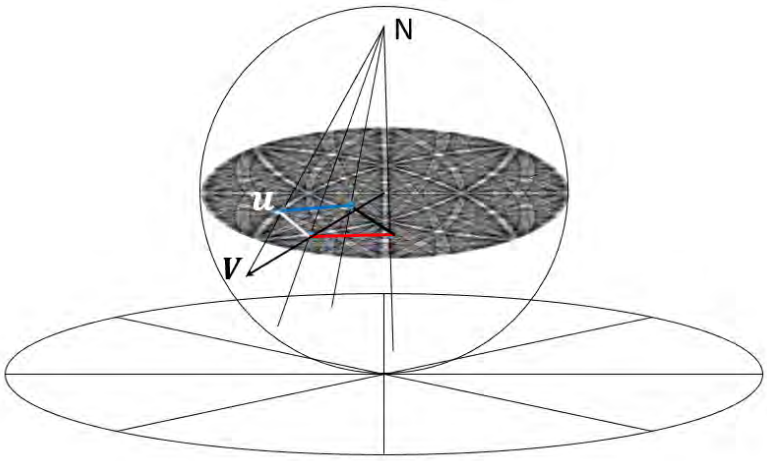

(a)

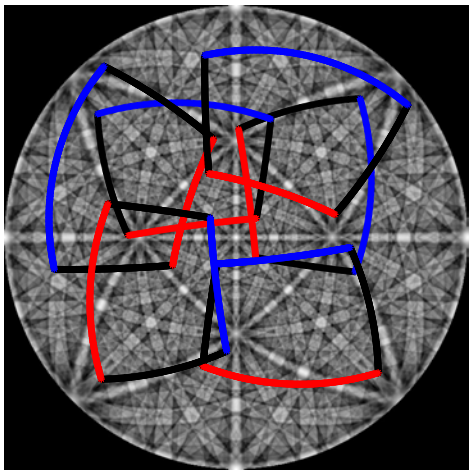

(b)

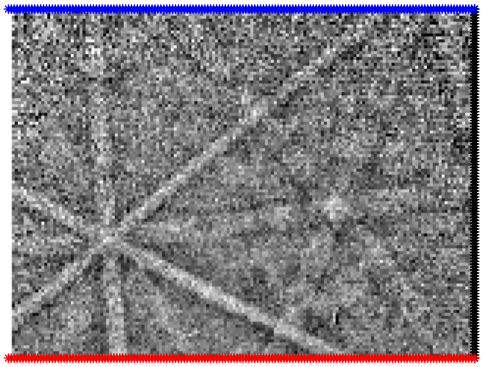

(c)

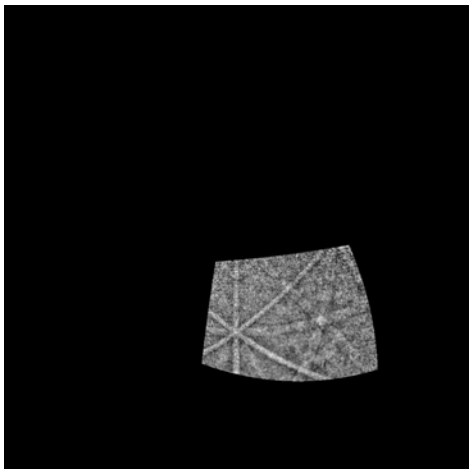

(d)

Figure 2: (a) Sketch of spherical projection of EBSP. (b) Several zones on the master pattern that will lead to simulated EBSP. (c) The corresponding experimental EBSP. (d) Master pattern generated by projecting the experimental EBSP back to the sphere.

The vector spaces $\boldsymbol{x}, \boldsymbol{w}, \boldsymbol{v}, \boldsymbol{u}$ adopted in the algorithm are summarized in Figure 3. The blue lines in Figures 3b-3d mark the evolution of the experimentally projected area in the algorithm operations. The changes of bases between $\boldsymbol{x}, \boldsymbol{w}, \boldsymbol{v}, \boldsymbol{u}$ can be done freely thanks to Equations 1 to 4.

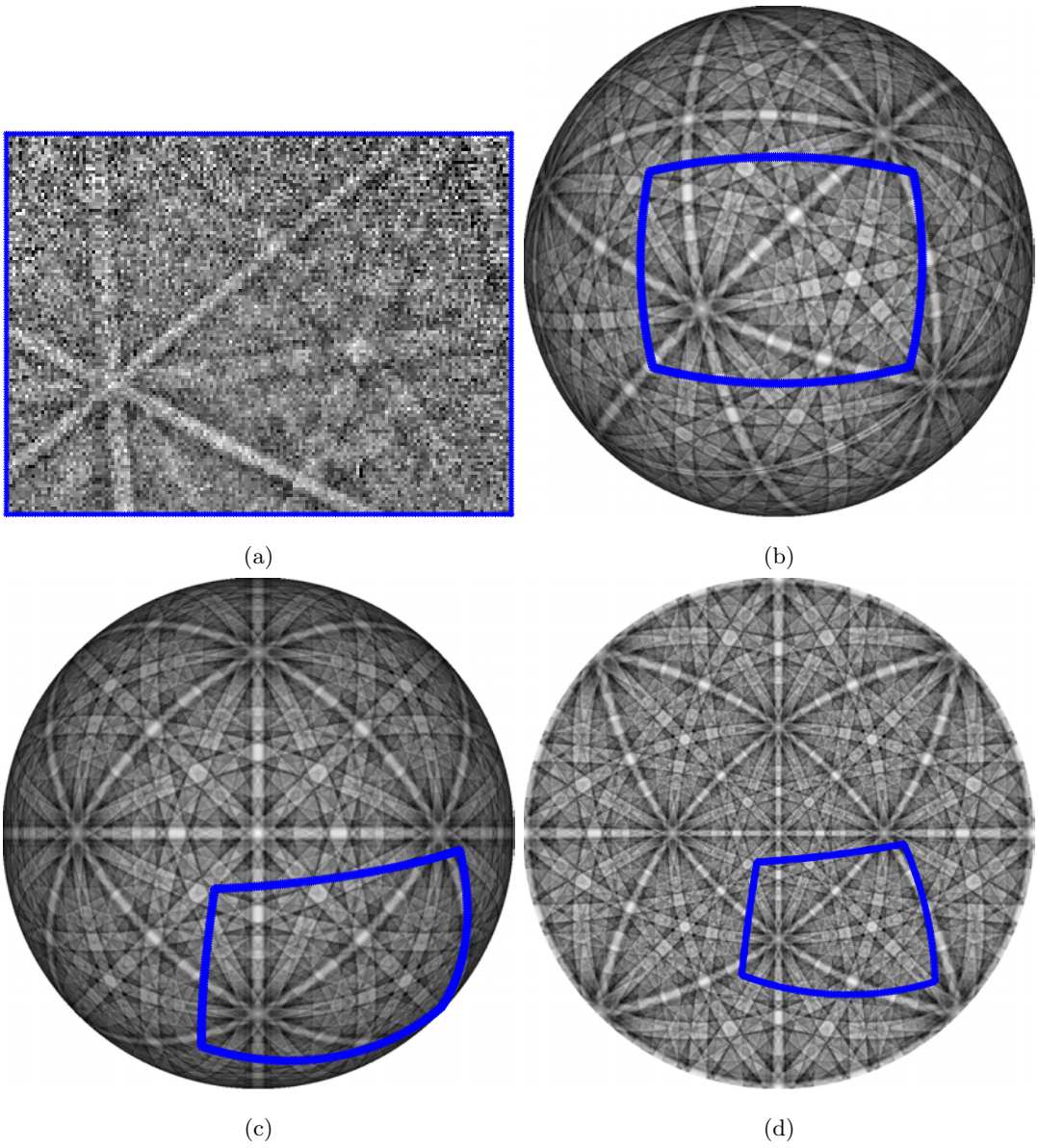

Figure 3: 4 domains described in the IDIC EBSD calibration algorithm. (a) 2D $\boldsymbol{x}$ space of the experimental EBSP. (b) 3D $\boldsymbol{w}$ space of the sphere master pattern in the experimental EBSP configuration. (c) 3D $\boldsymbol{v}$ space of the sphere master pattern in standard orientation. (d) 2D $\boldsymbol{u}$ space of the spherically projected master pattern. The blue lines in (b-d) outline the boundaries of the experimental EBSP.

We have hereby shown the steps to project the master pattern to a 2D detector with 6 parameters. They can be simply reversed to compute a master pattern from an experimental EBSP.

$$\boldsymbol{v} = \boldsymbol{n} - \frac{2(\boldsymbol{u} + \boldsymbol{n})}{(1 + |u|^2)} \tag{5}$$

and $\boldsymbol{w} = \boldsymbol{Q}^\top \boldsymbol{v}$.

Using equation (2), the expression of $\boldsymbol{x}$ is found

$$\boldsymbol{x} = \boldsymbol{x}^* - \frac{z^*}{\boldsymbol{w}.\boldsymbol{e}_z}\boldsymbol{w} \tag{6}$$

The mapping $\boldsymbol{u}(\boldsymbol{x})$ or its inverse $\boldsymbol{x}(\boldsymbol{u})$ allows one to navigate between the detector screen and the master pattern. An example of an experimental EBSP projected back to the master pattern is shown in Figure 2d.

Note that due to crystal symmetry, several Euler angle configurations can lead to the same EBSP. For example, all the marked rectangles in Figure 2b can lead to the same simulated EBSP resembling the experimental EBSP shown in Figure 2c.

Conventional DIC consists in correlating two gray level images, one of the reference state $f(\boldsymbol{x})$ and the other one of the deformed state $g(\boldsymbol{x})$. In the herein proposed algorithm, experimental EBSP is taken as $f(\boldsymbol{x})$ and the dynamically simulated EBSP master pattern $g(\boldsymbol{u})$. Note that contrary to conventional DIC and integrated DIC, the displacement field $\boldsymbol{u}(\boldsymbol{x})$ between the two images is not sought here, since the spherical projection distorts the displacement significantly.

Therefore the corrected deformed image corresponds to $g_{\boldsymbol{u}}(\boldsymbol{x}) = g(\boldsymbol{u}(\boldsymbol{x}, \boldsymbol{P}))$. The IDIC algorithm involves matching at best $f(\boldsymbol{x})$ and $g_{\boldsymbol{u}}(\boldsymbol{x})$, through the minimization of a quadratic norm of the residual r summed over the entire ROI. The cost function to minimize is written

$$\Theta = \sum_{ROI} \omega(\boldsymbol{x})^2 \left[f(\boldsymbol{x}) - g_{\boldsymbol{u}}(\boldsymbol{x}) \right]^2 \tag{7}$$

where $\omega(\boldsymbol{x})$ is the weight associated to each pixel $\boldsymbol{x}$, $g_{\boldsymbol{u}}(\boldsymbol{x})$ is the current estimate of simulated EBSP during iterative algorithms. The weights ω are introduced here as they may be used to make this functional *optimal* with respect to the handling of noise. This point will be made explicit later in Section 5. Before addressing this question, one may consider for instance a uniform weight $\omega(\boldsymbol{x}) = 1$, as is done in most common DIC analyses. The minimization of the cost function leads to successive corrections of the transformation $\boldsymbol{u}(\boldsymbol{x})$ estimation until convergence [42]. Starting from an approximate solution, the transformation $\boldsymbol{u}(\boldsymbol{x})$ is progressively corrected with linear combinations of sensitivity fields constituting the kinematic basis. For the proposed algorithm, IDIC is the chosen tool to registering diffraction images.

Note that in the EBSD calibration community the (normalized) dot product [24, 22] and cross-correlation [23, 26] coefficient have been commonly adopted to quantify the correlation between EBSPs, here we propose to adopt the least-square structure.It has been demonstrated that all the three aforementioned methods are equivalent [43] in the limit of very large images. However, the above criterion can be shown to coincide with the maximum likelihood, in situations where a Gaussian white noise is the limiting factor. Hence it achieves the minimal uncertainty (for all EBSP sizes). Moreover the weighted quadratic difference still minimizes the uncertainty in the case of Gaussian white noise with spatially varying variance.

2.2 Solution

The formulation of projecting EBSPs from a master pattern has been explored by several studies, and the present work focuses specifically on improving the full pattern matching by IDIC. The minimization algorithm follows the standard IDIC steps without major modification [42]. The cost function (7) is iteratively minimized with a Gauss-Newton algorithm.

A slight modification of any parameter δP_i, induces a modification of the corrected deformed image as

$$\delta g_{\boldsymbol{u}}(\boldsymbol{x}) = \nabla_{\boldsymbol{u}} g(\boldsymbol{u}) \cdot \frac{\partial \boldsymbol{u}(\boldsymbol{x}, \boldsymbol{P})}{\partial P_i} \delta P_i \tag{8}$$

The column vector $\{\boldsymbol{\delta P}\}$ gathering all corrections to $\boldsymbol{P}$ is obtained

$$[\boldsymbol{M}]\{\boldsymbol{\delta P}\} = \{\boldsymbol{\gamma}\} \tag{9}$$

where $[\boldsymbol{M}]$ is the Hessian matrix of size 6×6 at iteration $n-1$

$$M_{ij}^{(n-1)} = \sum_{ROI} \omega(\boldsymbol{x})^2 \left[\boldsymbol{\nabla} g(\boldsymbol{u}) \cdot \frac{\partial \boldsymbol{u}(\boldsymbol{x}, \boldsymbol{P})}{\partial P_i}\right] \left[\boldsymbol{\nabla} g(\boldsymbol{u}) \cdot \frac{\partial \boldsymbol{u}(\boldsymbol{x}, \boldsymbol{P})}{\partial P_j}\right] \tag{10}$$

and the second member $\{\boldsymbol{\gamma}_i\}$ includes the residual field

$$\gamma_i^{(n)} = \sum_{ROI} \omega(\boldsymbol{x})^2 \left(f(\boldsymbol{x}) - \widetilde{g}_{\boldsymbol{u}}^{(n)}(\boldsymbol{x}, \boldsymbol{P})\right) \boldsymbol{\nabla} g(\boldsymbol{u}) \cdot \frac{\partial \boldsymbol{u}(\boldsymbol{x}, \boldsymbol{P})}{\partial P_i} \tag{11}$$

When $\|\{\boldsymbol{\delta P}\}\| < \epsilon$, ϵ being chosen equal to 10^{-6} for all the calculations of this paper, the minimization stops and $\boldsymbol{P}$ is stored. Otherwise, $\boldsymbol{P}$ is updated

$$\boldsymbol{P}^{(n)} = \boldsymbol{P}^{(n-1)} + \boldsymbol{\delta P}^{(n)} \tag{12}$$

Once $\boldsymbol{P}$ is obtained, the simulated EBSP resembles the reference experimental EBSP.

The above explained algorithm is named IDIC EBSD calibration method. The conventional IDIC EBSD calibration has the potential to retrieve 6 parameters, and this number can be reduced freely. For example, if reliable PC values are already available, we can exclude them from the list of parameters to be optimized and focus on identifying Euler angles only. This operation can reduce the uncertainty significantly, as shown in Sections 4 and 5. One can also set any subset of parameters (for instance x^* only) that would be known and trusted in advance, and then optimize the remaining degrees of freedom.

The IDIC EBSD calibration algorithm has been implemented in Matlab, and was used for all the further reported results labelled IDIC. The proposed algorithm has been tested on two virtual EBSP data and two sets of experimental data: Two sets of virtual electron patterns with different noise levels and pattern sizes are tested to determine the precision of the algorithm. The first experimental test evaluates the algorithm performance on high-resolution EBSPs of a polycrystal sample, showing the satisfactory calibration results, and the high tolerance of the algorithm about sample tilt angles. The second test evaluates the application of the algorithm to a more realistic case, that is fast EBSD acquisition on a more complex polycrystalline material. In both experimental cases, the precision of Euler angles retrieved by IDIC EBSD is compared with the results obtained with commercial EBSD indexing software.

3 Test on virtual EBSPs with different noise levels and EBSP sizes

In order to evaluate the performance of IDIC EBSD calibration method in the presence of random noise, a set of 10 virtual EBSPs of size 240×320 with different noise levels is generated, as shown in Figure 4. The simulated EBSP corresponds to face-centered-cubic Al crystal, and 8 bits gray level depth is used. On top of the simulated EBSP,

uniformly distributed noise levels 2^{i-1} $(i = 1, 2...10)$ is added, so the noise levels form a geometric series. Note that for final virtual EBSPs the noise level is much higher than the signal, as can be seen from Figure 4.

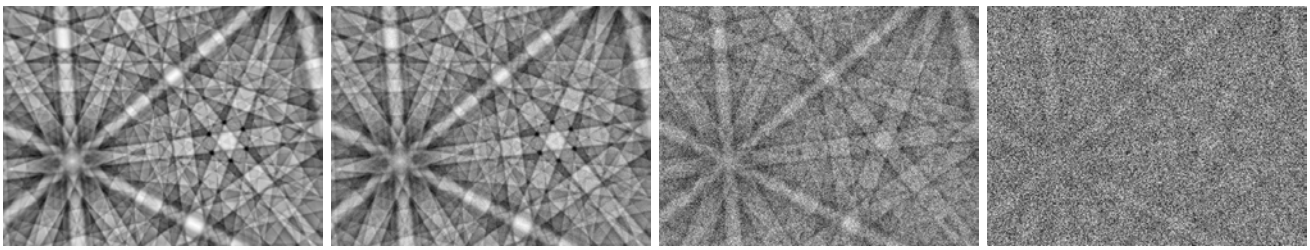

Figure 4: Examples of virtual EBSPs with noise levels 2, 5, 8 and 10

The initiation value of the IDIC EBSD calibration parameters is intentionally perturbed from the exact one. The initial PC value is 5 pixels off from the ground truth, and the initial Euler angles is moved 0.7° away from the ground truth. Two independent projection areas (labelled 1 and 2 in the following) can be chosen, as shown in Figure 5a, and they correspond to the same crystal orientation due to cubic crystal symmetry. The difference of the projected EBSP from zone 1 and 2 is shown in Figure 5b, which shows the magnitude of the interpolation error. Note that the modified Lambert projection proposed in Ref. [36] has also been tested, and a similar phenomenon persists. IDIC EBSD calibrations are performed choosing either one of the two projection areas, and a third one is based simultaneously on the two projection areas. The entire computation is repeated for 15 different noise samplings to study the distribution of calibration error.

The mean calibration error, together with its standard deviation, are plotted in Figure 5c for PC values and in Figure 5d for Euler angles. PC error is defined as the distance in 3D space between the ground truth and the calibrated values, and Euler angle error is the misorientation between the ground truth and the estimated values. The noise level 0 in Figure 5c and Figure 5d corresponds to the simulated EBSP with no noise. It is found that when the applied noise level is very low or absent, the calibration error is almost flat. This is a clear indication that the interpolation error, which originates from the spherical projection distortion of subpixel query points, dominates the calibration error. When larger EBSP and master patterns are analysed, this interpolation error of subpixel query points decreases, as will be demonstrated further down. Yet, with higher noise level, a power-law relationship between the noise level and the calibration error is observed. Even when the noise level appears to compete significantly with the meaningful signal, Figures 5c and 5d show that PC evaluation and Euler angle measurements are at most affected by uncertainties of order a few pixels and less than 1 degree respectively. This level of uncertainly is not that different from those obtained today with conventional EBSD analyses, and hence such results may trigger the recourse to high speed EBSD analyses when a low precision is tolerable.

Another interesting point is that when the applied noise level is very low, the projection area 1 leads to consistently lower calibration error than area 2. This is due to the fact that area 1 is closer to the central area, where the distortion effect of spheric projection is smaller. This phenomenon disappears when the interpolation error is dominated by the applied artificial noise.

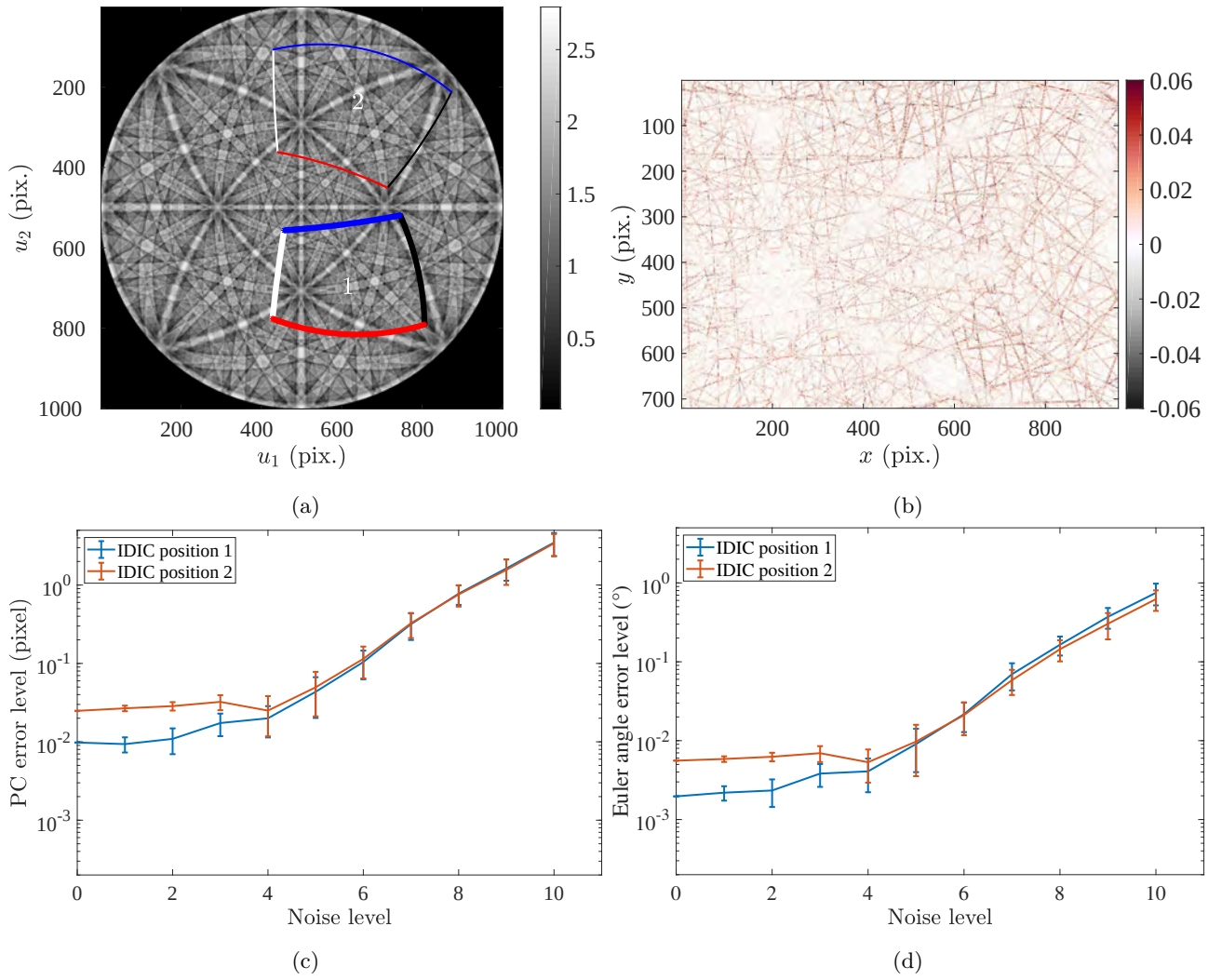

Figure 5: (a) Projection areas adopted to calibration virtual EBSPs. (b) Error of interpolation shown as the difference between EBSPs projected from zone 1 and 2. IDIC EBSD calibration error in function of noise level for PC values(c) and Euler angles(d).

Another important parameter for EBSD calibration is the size of experimental and simulated patterns. A series of EBSPs of different sizes and with the same noise level is generated, and the top row of Figure 6 shows the EBSPs of 80×60, 160×120, 320×240 and 800×600. The noise level is set as 1/9 of the dynamic range of EBSP, that corresponds to 2^5 in the previous analysis and the same as the experimental EBSP noise level as characterized in Ref. [13]. Master patterns of size 251×251, 501×501, 1001×1001 and 2001×2001 (see bottom row of Figure 6) simulated by EMsoft are used for the comparison, and their calibration results are shown in Figure 7. It is found that for EBSPs smaller than 160×120, the performances of all master pattern sizes are equal. The calibration error level and the EBSP size are related by a power-law relation, especially for the line of 2001×2001 master pattern. As the EBSP size increases, the curves of smaller master pattern deviates from the power-law. For 251×251 master pattern the separation takes place for an EBSP length of order 200, and for 501×501 master pattern this transition occurs at about 600. For 1001×1001 master pattern, the separation starts near EBSP length 2000, which is already

the maximal experimental EBSP size. After the separation, the curves are flat, indicating that larger EBSP size does not improve calibration precision if insufficient master pattern is adopted. Thus it is suggested that for the smaller EBSPs (say 160×120) one may choose smaller master patterns, such as 501×501, to save computation time. For EBSPs larger than 800×600, the master pattern of size 2001 lead to lowest calibration error. This rule of thumb is obeyed by all the following tests on experimental EBSPs.

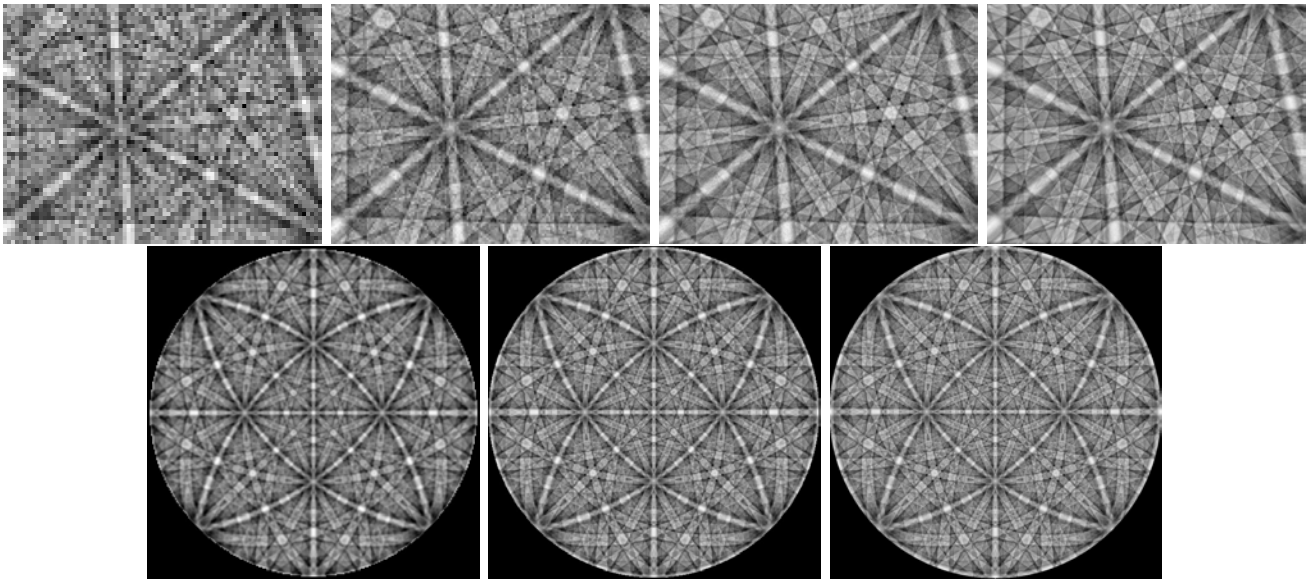

Figure 6: Top row: examples of virtual EBSPs of different sizes and with the same noise level. From left to right, the image width is 80, 160, 320 and 800 (whereas its height is 60, 120, 240 and 600). Bottom row: master pattern of size 251, 501 and 1001 respectively.

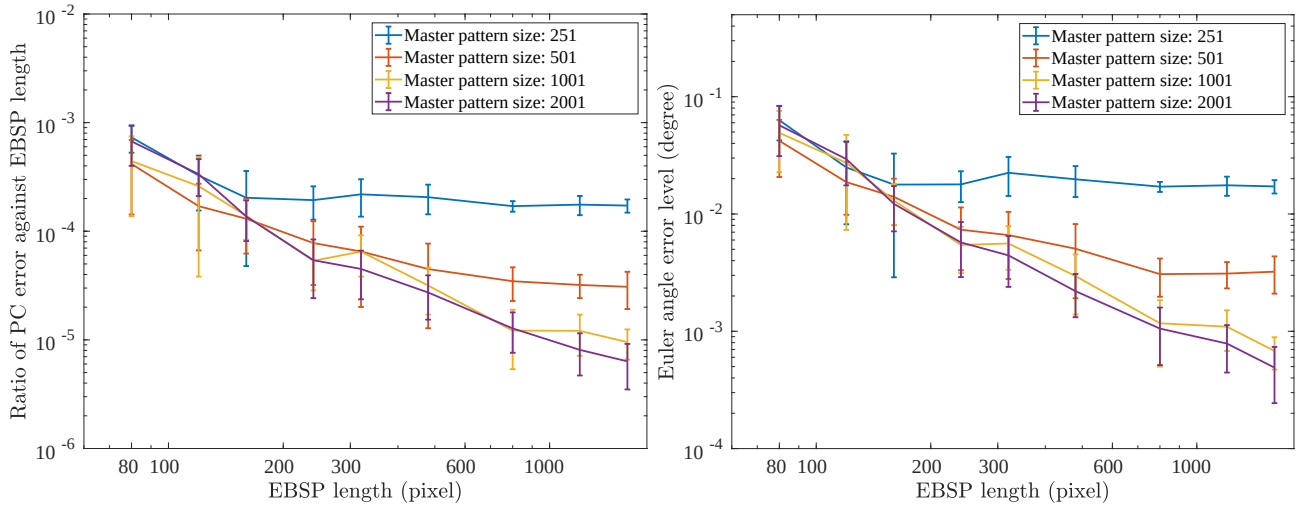

(a) (b)

Figure 7: IDIC EBSD calibration error in function of the size of EBSP and master pattern for PC values(a) and Euler angles(b).

It is worth noting that as the EBSP size grows, the calibration error reduces and stabilizes for master patterns

smaller than 1001. In our calculation the calibration error does not pick up when the EBSP size is larger than 600×800, as reported previously by Friedrich *et al.* [28]. This is a clear demonstration of the stability of the proposed algorithm.

The effect of crystal lattice distortion, due to elastic strain, on IDIC EBSD calibration results is also studied on simulated EBSPs. A series of EBSPs of size 1024×1344, corresponding to Euler angles (352.8°, -103.0°, 72.8°) are generated by EMsoft with varying ϵ_{12} and ϵ_{23} levels up to 0.2%. These EBSPs are then calibrated by the proposed algorithm. As the current algorithm assumes that the EBSPs are stress-free, the calibration results will be drifted from the true value. The deviation of PC and Euler angles due to the two elastic strain components are shown in Figure 8. Up to the yielding point, elastic strain will lead to error in crystal orientation below 0.1° and PC error in the order of pixels. Besides, for each PC component the drift is linear with the strain level. As a result, for EBSD acquisitions where the elastic strain is centered on zero, the average PC drifts will also be close to zero. In this case, PC errors due to elastic strain could be effectively mitigated by a global filter on the PC fields.

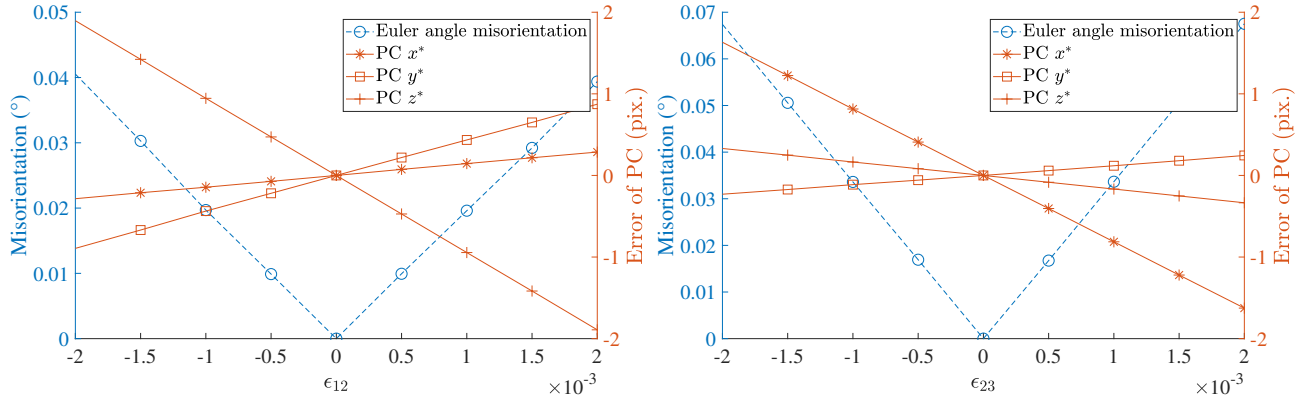

Figure 8: IDIC EBSD calibration error in function of the elastic strains for different values of ϵ_{12} (a) and ϵ_{23} (b).

Last but not least, let us emphasize the very low calibration error level when adopting large stress-free *simulated* EBSPs and master pattern (2001 pixel wide): below 10^{-5} of the EBSP length for PC calibration and below 10^{-3} degree for Euler angles.

4 Performance on a full resolution EBSD acquisition

An experiment was performed to test the proposed EBSD calibration method on an Al-Mg alloy (6 wt.% Mg). The sample is mechanically polished and chemically etched to prepare for the EBSD acquisition. High definition (1200× 1600 pixels) diffraction patterns recorded by Bruker e$^-$*Flash*^{HD} EBSD detector are analysed to provide a 150×200 map of crystalline orientation, resolved at a step size of 1.625 µm. The acceleration voltage is 20kV. The probe current was 20 nA, and the dwell time was 0.9 s.

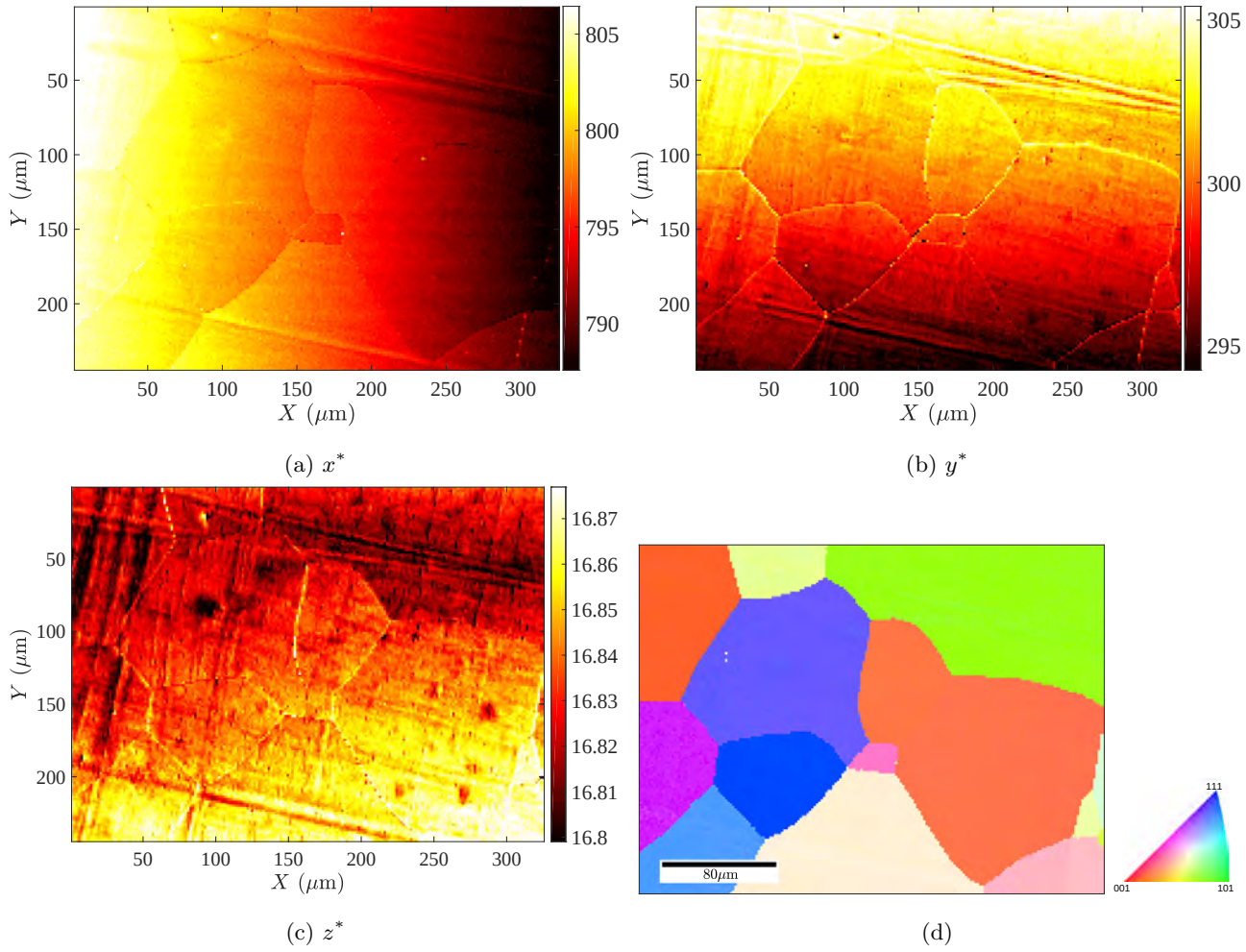

(a) x^* (b) y^*

(c) z^* (d)

Figure 9: (a-c) Calibrated pattern center coordinates x^* (in pix.), y^* (in pix.) and z^* (in **mm**) fields for the AlMg alloy. Inverse pole figure of the polycrystal is shown in (d).

Figure 9 shows the calibrated pattern center fields for each EBSP. x^* field exhibits mainly a rather homogeneous gradient along the X axis. There are also clear variations in y^* and z^* fields, with a gradient mostly along the Y axis, onto which linear and singular features are superimposed. These full field PC values resemble those of single crystal Si [44, 39], although the present work is more demanding as the sample is less perfect. It is worth noting that z^* field is lower in the top area and higher in the bottom one. This is related to the scanning order: the lower part of the sample is indexed in the first place, where it is closer to the EBSD detector. This is in accordance with the y^* field, where the top is brighter. Linear fitting of x^* field shown in Figure 9a demonstrates that the pixel size of the EBSP detector is 19.2 µm. The reference pixel size, according to the manufacturer of the detector, is 20 µm, which means our prediction is 4% smaller.

The inter-granular straight traces are due to polishing artifacts/scratches and appear in all three PC fields, especially in y^* and z^* as shown in Figures 9b and 9c. Those traces mainly exist in two perpendicular directions, because in the sample preparation procedure, the sample is polished along two vertical directions with abrasive paper of different grades. The variations of z^* up to 20-40 µm cannot be attributed to the surface topography, or to an electron channelling phenomenon. This pixel-level PC component drift is most probably due to elastic strain, as

illustrated in Figure 8. This phenomenon demonstrates that the IDIC EBSD calibration is very sensitive to elastic strain, and the estimated PC fields readily highlights the strained area.

The Kernel Average Misorientation (KAM), or local misorientation, is a property that characterizes the local deformation level of a crystal. In the present case, the KAM is defined as

$$\texttt{KAM}(\boldsymbol{X}) = \langle \varphi(\boldsymbol{R}(\boldsymbol{X}) \cdot \boldsymbol{R}(\boldsymbol{Y})^{-1}) \rangle_{\boldsymbol{Y}} \tag{13}$$

where $\boldsymbol{R}(\boldsymbol{X})$ is the rotation tensor calculated at point $\boldsymbol{X}$, $\boldsymbol{Y}$ denotes generically all neighbours to $\boldsymbol{X}$, and $\langle ... \rangle_{\boldsymbol{Y}}$ indicates an average over $\boldsymbol{Y}$. In the present case, the neighbourhood is limited to the four nearest neighbours. Finally,

$$\varphi(\boldsymbol{R}) = \text{Arccos}\left(\frac{\text{tr}(\boldsymbol{R}) - 1}{2}\right) \tag{14}$$

is the function that computes the misorientation angle from the rotation $\boldsymbol{R}$. Note that in the present study the misorientations higher than 3° are excluded from KAM calculation, as they occur only at grain boundaries.

Figure 10a shows the KAM field provided by Hough-based HKL Channel5, while Figure 10b shows the KAM field of the first IDIC EBSD calibration passage where the PC is determined freely. Note that their coloring scale is different, and the very high noise in Figure 10a hinders the characterization of fine structures. Then, the PC field is fitted to a plane, and supposing the indexed points form a linear grid on the sample surface. This linear-planar fit can be summarized by $(x^*, y^*, z^*)^T \approx \boldsymbol{q}(X, Y, 1)^T$, where $\boldsymbol{q}$ is a 3×3 matrix. The linear-regressed PC field, noted hereafter as (x^{*R}, y^{*R}, z^{*R}), is prescribed in a second pass that refines the Euler angles denoted by $(\varphi_1^R, \phi^R, \varphi_2^R)$. The low uncertainty of the current calibration algorithm allows one to obtain a global view of the PC fields, and decide for an appropriate filter. For example, a median filter would be more fitted for a very rough-surface sample. As a result, this *a posteriori* filtering of PC field is different to the *a priori* one adopted in Ref.[22]. The resulting KAM field is shown in Figure 10c. Setting PC values and focusing on refining Euler angles reduces the orientation indexation error by 15%. Note that this second-round calibration with fitted PC fields is by nature different from the post-indexing filtering of Euler angle as proposed in Ref. [45], as the current algorithm improves the crystal orientation precision by cutting down the non-physical high-frequency PC variations, thus do not compromise the spatial resolution of EBSD. The influence of linear-regressed PC on the calibrated crystal orientation is shown in the histogram 10d, together with the Euclidean distance of PC fields before and after the regression shown in histogram 10e. In both histograms the bin number are 200, and 'ratio of hits', or relative frequency, is defined as the number of hits divided by the total EBSD acquisition points. This information will be compared to the second experimental dataset.

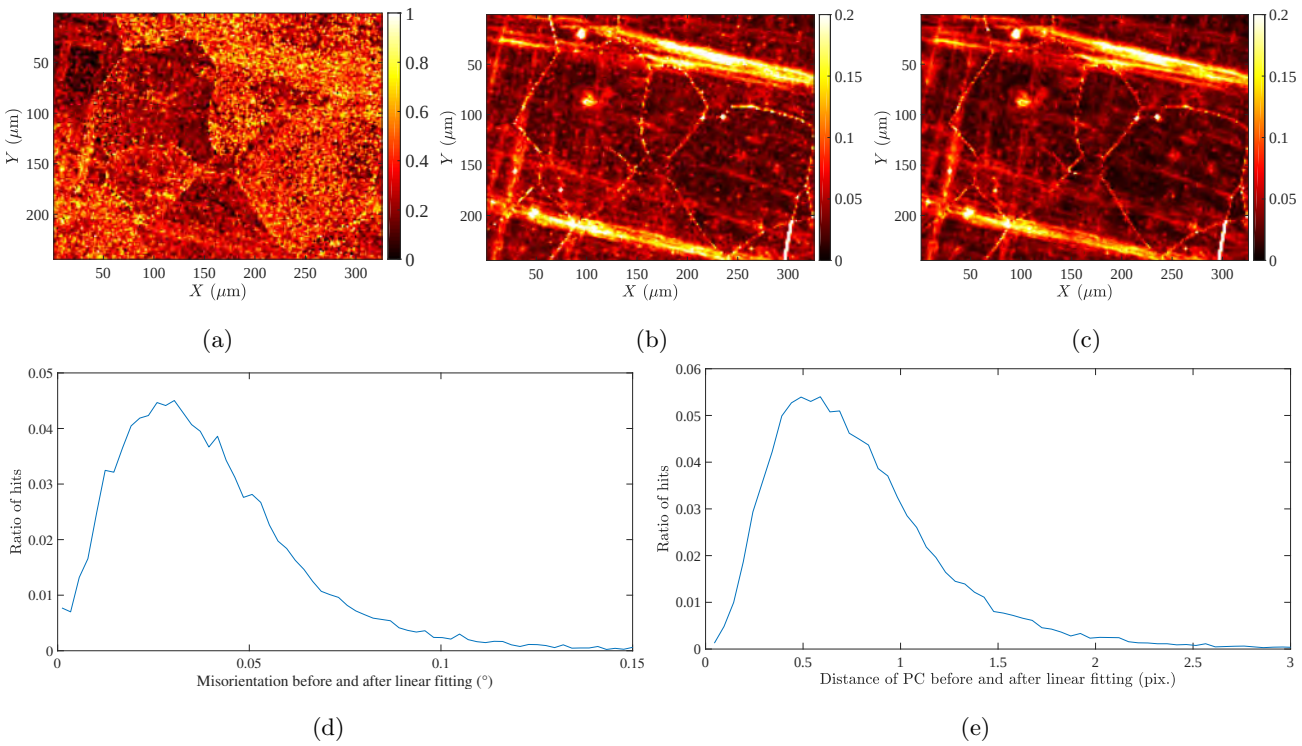

Figure 10: Kernel average misorientation in ° for the EBSD acquisition, with Hough-based EBSD (a), IDIC EBSD calibration with floating PC (b) and IDIC EBSD with PC values fitted to a linear spatial dependence (c). Histogram of misorientation (d) and PC distance (e) before and after the linear fitting.

A series of EBSD has been acquired with different sample tilt angles (70° and 65°) on the same sample area, in order to demonstrate the correctness of the indexation algorithms. Figures 11a-11b show the EBSPs of the same sample point while tilted at 70° and 65°respectively. The band positions change with the tilt angle, as the Euler angle values are changed in the EBSP detector reference. Besides, the pattern quality deteriorates as the tilt angle deviates from 70°, especially for the lower part of the pattern. The inverse pole figure of the 5-grain indexed region is shown in Figure 11c. All the EBSPs are indexed by both Hough-based algorithm `HKL channel 5` with the correct tilt angle being provided and our IDIC EBSD calibration method. The misorientation field between the EBSD acquisitions evaluated by `HKL channel 5` is shown in Figure 11d. The misorientation angle obtained by IDIC EBSD calibration between EBSD tilt of 65° and 70° with floating PC is shown in Figure 11e, while the same field retrieved with prescribed linear PC fields is shown in Figure 11f. The misorientation angle estimated by IDIC EBSD calibration fluctuates around the expected 5°, which is the difference of the tilt angles. Hough-based indexation leads to misorientation varying between 0.1° and 1.3°. This test shows the high consistency of the IDIC EBSD calibration method, especially as compared to the Hough-based indexation. Besides, prescribing linear PC fields reduces the misorientation, as shown in Figure 11g. The standard deviation of misorientation angle by IDIC EBSD calibration is 0.042° with prescribed linear PC estimate. It is evident that our IDIC EBSD calibration algorithm leads to much more consistent crystal orientation indexation. This test also demonstrates that our algorithm is more tolerant to various sample tilt angles in EBSD acquisition, which is the case for rough surface samples, while a single tilt angle needs to be provided to other EBSD indexation methods. The high tolerance of tilt angle is quite

as anticipated, as the sample tilt is not involved intrinsically in the proposed algorithm.

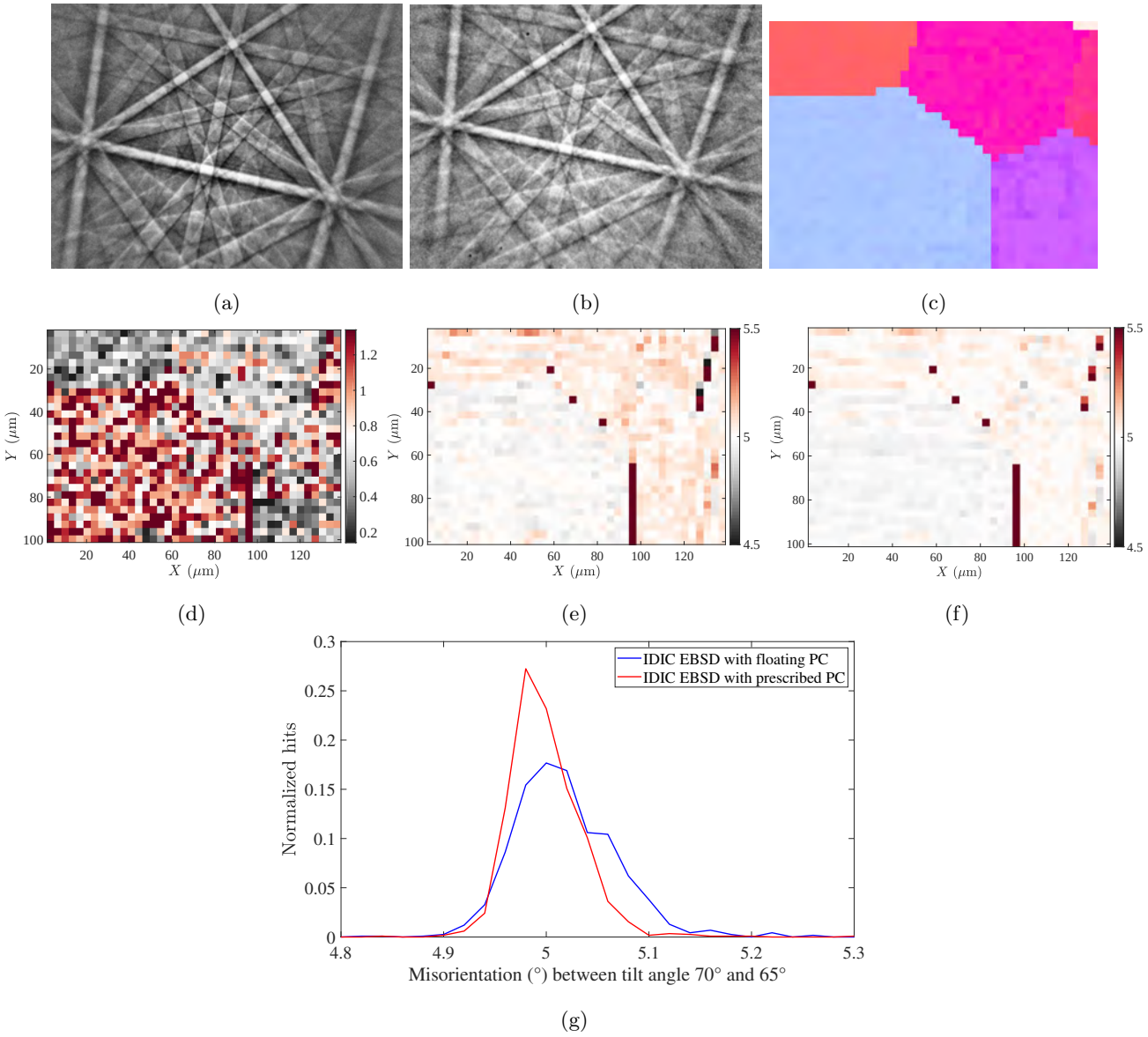

Figure 11: (a-b) EBSP of the same position with sample tilt 70° and 65° respectively. Inverse pole figure of the polycrystal is shown in (c). (d) Misorientation in ° between two crystal indexations of sample tilt 65° and 70° obtained by Hough-based `HKL Channel5`. The same field calculated by IDIC EBSD calibration with floating PC (e) and linearly fitted PC values (f). (g) The histogram of the misorientations in (e) and (f).

The performance of IDIC EBSD calibration is compared to two other full pattern matching methods, namely the evolution algorithm adopted by [27] and the commercial software ESPRIT DynamicS. The EBSPs of the last column shown in Figure 11c are calibrated. The evolution algorithm adopted here uses the same projection function as IDIC EBSD, with the same 6 parameters. Population of each generation is set to 5, and the crossover probability 0.9, mutation factor 0.5. The evolution algorithm is stopped when the cross-correlation c between the experimental and the simulated EBSP increases less than 10^{-6} in 20 consecutive generations ($c(i) - c(i-20) < 10^{-6}$). The

calibrated PC values by the three methods are shown in Figure 12. The three methods roughly result in the same PC levels, yet the calibration uncertainty to a plane surface is 84, 2.6 and 0.64 pixels for DynamicS, evolution algorithm and IDIC EBSD calibration respectively. The computing time is 10 seconds, 5 minutes and 30 seconds for the three methods respectively. IDIC EBSD calibration outperforms the other two methods, and achieves good combination of precision and speed.

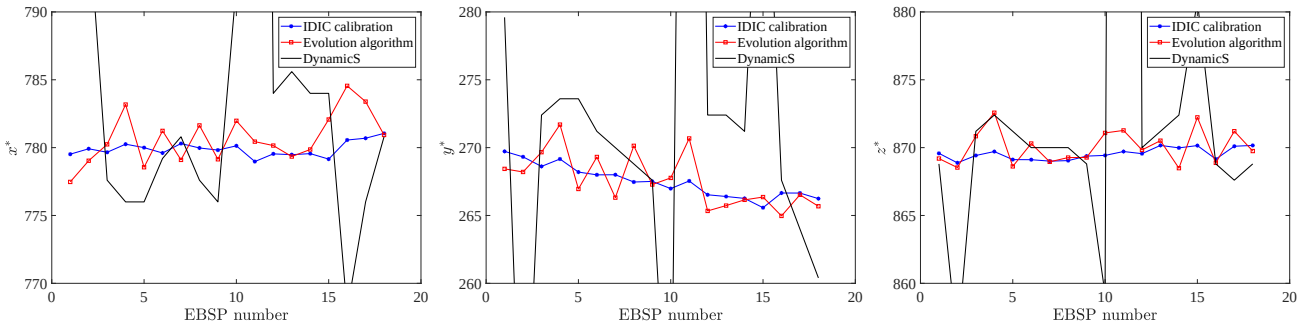

(a) (b) (c)

Figure 12: Comparison of pattern center x^* (a), y^* (b) and z^* (c) obtained by three full pattern matching methods: IDIC EBSD calibration, evolution algorithm and ESPRIT DynamicS.

5 Performance on a fast EBSD acquisition of an in-situ tensile test

A more demanding experiment was performed to test the robustness of the proposed EBSD calibration method for an in-situ mechanical test where EBSPs were acquired with a poor definition and at a fast rate, thus with a high noise level. An Al-(6 wt.%) Mg sample was electro-chemically polished and subjected to an *in-situ* tensile loading inside the chamber of a Tescan Lyra3 SEM (Figure 14a). An in-situ rig (Kammrath-Weiss) was used for performing the tensile test. The loading direction is horizontal in Figure 14a and the loading rate was 10^{-2} min^{-1}. All along the traction test up to 5%, 4 EBSD acquisitions were performed to study the evolution of the microstructure. The working distance for EBSD acquisitions was 16.3 mm, electron acceleration voltage was 20 kV, the probe current was 20 nA, and the dwell time was 0.03 s. EBSD patterns were recorded by Oxford Instruments NordlysMax3 camera with Aztec software, binned to 120×160 pixels, and each pattern was the result of averaging three frames. This acquisition speed and binning strategy represent the standard fast EBSD acquisition. A square area of 450 µm×450 µm was indexed, and the step size was 1.8 µm for the sample before tensile test and 0.9 µm after.

The proposed IDIC-based EBSD calibration was used again to process these data. Figure 13 shows an example of integrated correlation result on an EBSD acquisition. Figure 13a shows an EBSP of size 120×160, where noise is quite visible. After launching the IDIC EBSD calibration, the 6 projection parameters are estimated and a simulated EBSP close to experimental diffraction pattern is obtained, as shown in Figure 13b. No deliberately introduced noise was considered, and the average and variance values of the gray levels of the simulated pattern are simply set identical to those of the experimental one. The residual field (difference between Figure 13a and Figure 13b) is shown in Figure 13c. It is far from being composed of noise solely. The Kikuchi bands in the residual field are generally darker, and the area close to high-symmetrical axis zone is significantly brighter. This gray level

bias is due to the fact that master pattern is not capable to simulate the brightness of experimental EBSP. In fact, this systematic gray level difference can be corrected by projecting numerous experimental EBSPs back to the $\boldsymbol{u}$ domain to generate a master pattern as suggested by Ref. [46], then use this new master pattern for calibration.

In order to study the noise distribution of EBSPs, $\omega(\boldsymbol{x})$ is set as uniformly 1, and 176 residual fields of different grains are collected and analysed. The mean values and standard deviations for each pixel of the 176 residual fields are shown in Figure 13d and Figure 13e respectively. Some of the pixels are very bright, while some other pixels are consistently darker than average. There are also horizontal stripes with a spacing of 4 pixels in Figure 13d. This phenomenon is the readout artefact of the EBSP detector. Besides, a defect, (dark pixels outlining a curly shape in the bottom part of Figure 13d), reveals presumably a scratch of the EBSP detector. Whatever the interpretation, this systematic error field should be removed from each experimental EBSP of the acquisition. The noise level shown in Figure 13e is a good indicator of how much a corresponding pixel is to be trusted. For all the computations of the present paper, the inverse residual standard deviation is used as a weight, ω, for each pixel. Besides the mean value and the variance, the distribution type of the gray levels for each pixel also plays an important role in optimizing the calibration. Figure 13f shows the kurtosis, *i.e.,* 4th order moment of the pixel residual scaled by the square of its variance, $\langle (f - \langle f \rangle)^4 \rangle / \langle (f - \langle f \rangle)^2 \rangle^2$. The latter ratio should be exactly 3 for a Gaussian, roughly verified here. This piece of information indicates that a Gaussian (normal) distribution is a good approximation of the statistical distribution of residual values. It is in such cases that one can devise an optimal cost function, where the weight is the inverse standard deviation.

The weighting parameter $\omega(\boldsymbol{x})$ is set as the inverse of standard deviation shown in Figure 13e (eventually after a Gaussian smoothing). The effect of $\omega(\boldsymbol{x})$ is shown in Figure 13g. The dynamic range is kept the same between Figure 13a and 13g, and it is visible that the noise level has been reduced, especially in the upper area. The simulated EBSP is also weighted as shown in Figure 13h, and the resulting residual field is significantly lower (see Figure13i). This weighting operation reduces the orientation indexation uncertainty by 19%. (The KAM value reduces from 0.32° to 0.26°).

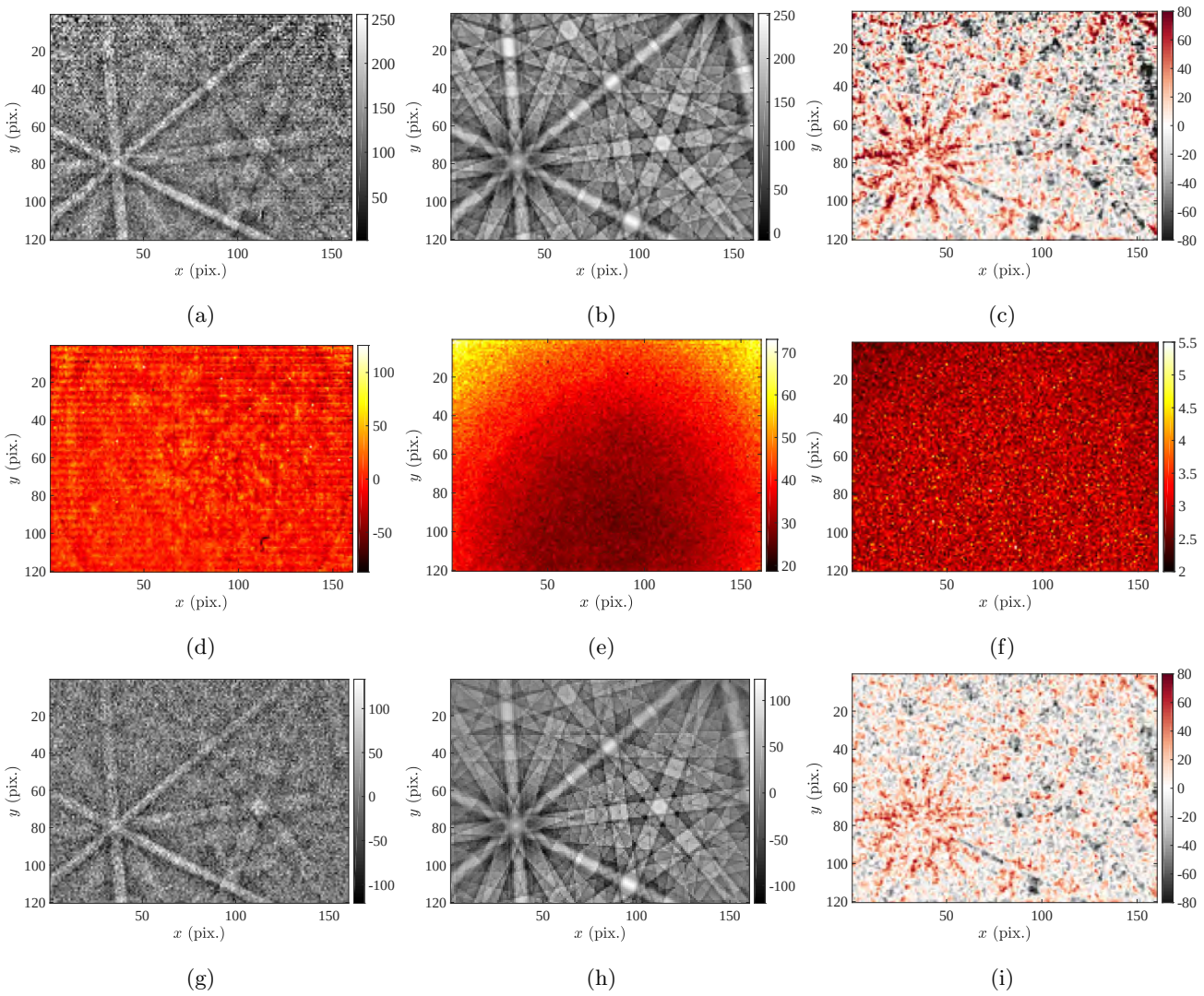

Figure 13: An example of IDIC EBSD calibration. (a) Experimental EBSP of size 120×160; (b) Simulated EBSP extracted from EMsoft master pattern; (c) Residual between (a) and (b); (d) Average residual field from 176 EBSP residuals, where dead pixels and horizontal stripes are visible; (e) Standard deviation and (f) Kurtosis of 176 EBSP residuals; (g) The experimental EBSP centered around 0 and modulated with the standard deviation shown in (e); (h) Weighted simulated EBSP; (i) The residual field between (g) and (h).

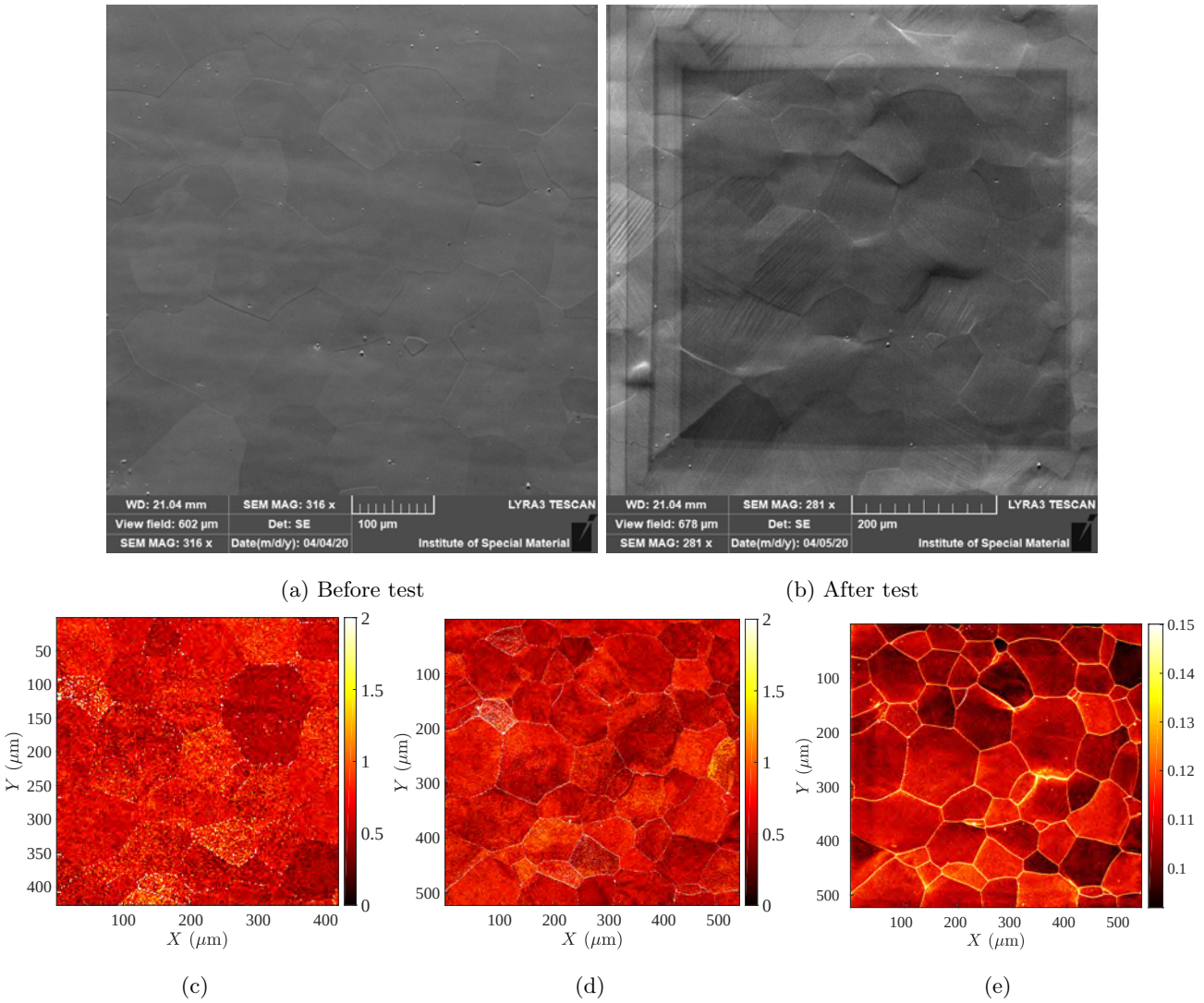

(a) Before test (b) After test

(c) (d) (e)

Figure 14: Secondary electron image of the sample before (a) and after (b) 5% tensile test. The misorientation (expressed in degrees) between the present algorithm and the Hough transformation based EBSD indexation before (c) and after (d) 5% strain. (e) Residual norm field for the EBSD after 5% strain.

To initialize the IDIC-EBSD calculation, the Euler angles retrieved by common EBSD software (Bruker, Channel5, EDAX) constitute a good initial choice for $\boldsymbol{P}$. To initialize the calculations with unindexed EBSPs, it is generally recommended to take the projection parameters of its immediate neighbours since the crystal orientation and pattern center are assumed to be close for nearby material points. If no Euler angles are available, it is suggested to resort to `DynamicS`, whose free-trial version provides Euler angles and pattern center with adequate precision[1].

The present algorithm calculates the Euler angles for the entire indexed area, and it is interesting to compare the crystal orientations estimated by conventional EBSD software and the proposed method. The misorientations between the two methods before and after the tensile test are shown in Figure 14c and 14d respectively. The misorientation before tensile test is more homogeneous inside each grain, while the misorientation levels across grain

[1]Note that initializations given by EBSD OIM software have to be rotated by a 70° rotation around the X-axis, as the EBSD OIM takes the sample inclination into consideration, while this step is not necessary when using DynamicS.

boundaries are clearly different. After tensile test, intra-grain misorientation appears and its distribution is related to the sample topography, as revealed by Figure 14b and 14d. The proposed algorithm allows a supplementary degree of freedom from the correction of pattern center, thus it is more tolerant to rough surface than conventional EBSD indexation methods, as demonstrated in Section 4. The residual norm field for the EBSD acquisition after tensile test is shown in Figure 14e. The residual level is higher at grain boundaries, where the EBSP quality is poor. Besides, the residual level for each grain is roughly homogeneous, yet it varies across grain boundaries. The previously analysed surface appears contaminated, (as can be seen in Figure 14b from the darker inner rectangle) and this pollution induces a higher residual level as can be seen in Figure 14e where the same rectangular region is visible on the residual plot.

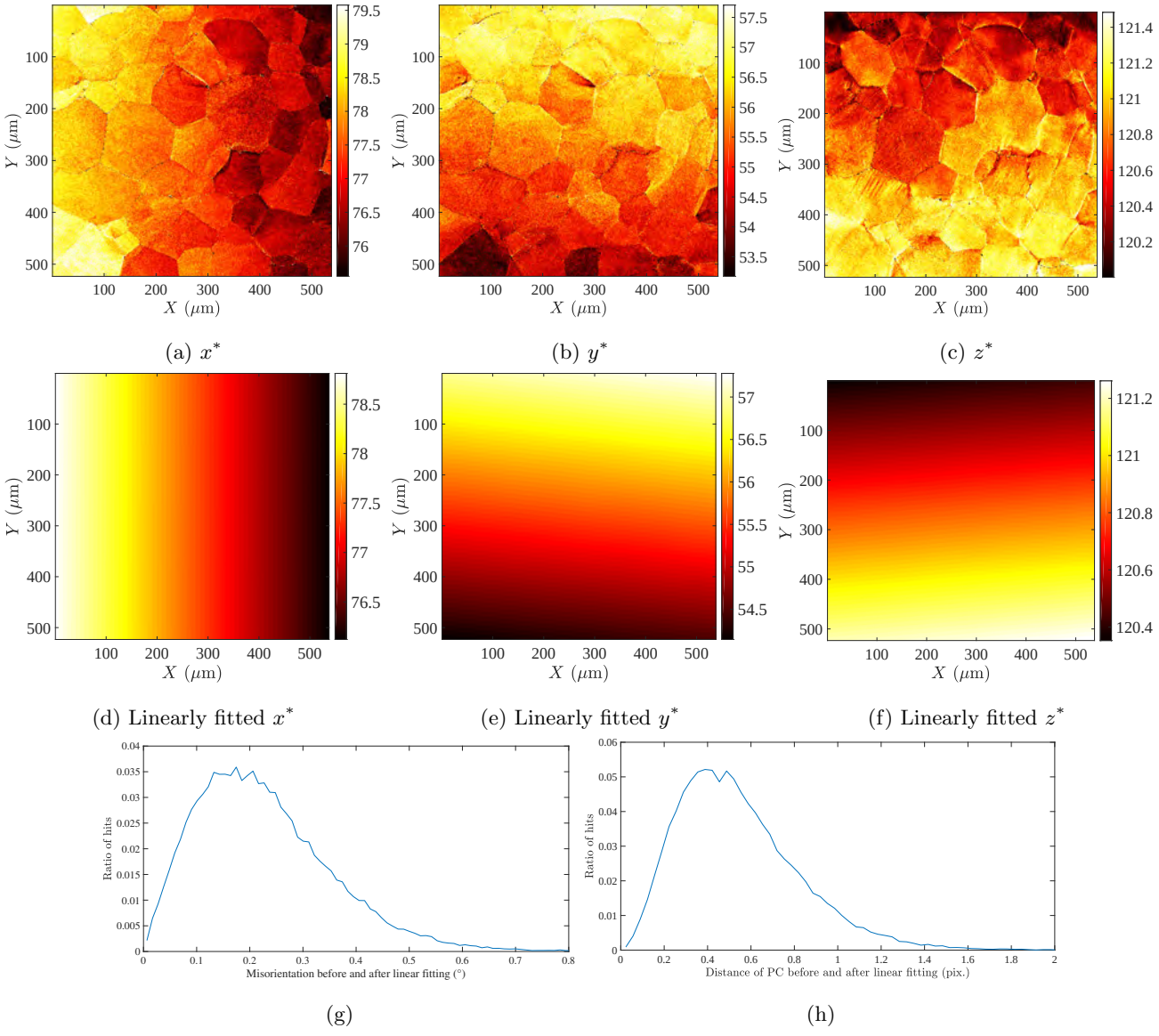

(a) x^* (b) y^* (c) z^*

(d) Linearly fitted x^* (e) Linearly fitted y^* (f) Linearly fitted z^*

(g) (h)

Figure 15: (a-c) Retrieved pattern center fields for the fast acquisition test case with 120×160 pixel EBSPs. (d-f): linearly fitted pattern center fields. Histogram of misorientation (g) and PC distance (h) before and after the linear fitting.

The computed pattern center fields are presented in up row of Figure 15. x^* field across grain boundaries is less continuous than in the previous high-definition test case (Section 4), but the global trends remain. This discontinuity of PC value field for different crystal orientations is also observed with other full EBSP pattern matching algorithms [22]. The PC steps at grain boundaries indicate the systematic errors of software-based EBSD calibration, mainly due to the unaccounted asymmetry of experimental Kikuchi bands [47] and inhomogeneous distribution of diffracted electron energy [48]. Inside each grain, the pattern centers fluctuate, yet the topography of the sample is clearly not sufficient to account for the observed variations, as confirmed qualitatively from SE images (Figure 14). As a result, a linear regression is applied on PC fields to mitigate the PC discontinuity, and the result is shown in the middle row of Figure 15. The linear fitting result suggests that a pixel of the NordylisMax3 detector is 50.04µm wide, 1% smaller than the reference value 50.6 µm provided by the manufacturer. This satisfactory result demonstrates the accuracy of IDIC EBSD calibration results.

In order to gain further precision for Euler angles, the filtered pattern centers were set fixed to their filtered value, and the IDIC EBSD calibration algorithm was run again to evaluate the Euler angles only. Only 3 degrees of freedom are left in the computation, thus the computing time and Euler angle uncertainty drops significantly. Figure 15g and 15h shows the histogram of misorientations and PC differences before and after the linear fitting. These plots show that the precision of the IDIC calibrated Euler angles is about 0.2°, and the precision of calibrated PC is about 0.5 pixel. Note that their comparison with Figure 10d, 10e shows that high-resolution EBSPs lead to a higher gain of PC calibration precision, and a lower gain in crystal orientation precision.

As illustrated in Figure 16a, the KAM provided by standard EBSD analyses (`Aztec` of Oxford Instrument) is too noisy to reveal a misorientation of the order of 0.1°. In contrast, considering the proposed calibration with 6 degrees of freedom, IDIC EBSD results in a lower misorientation level, as shown in Figure 16b, than Hough-based EBSD indexation. It is worth noting that the IDIC method leads to a more homogeneous KAM field than Hough indexation, which means that the precision of IDIC indexation method is less dependant on the crystal orientation.

GNDs can be estimated from kernel average crystal misorientations according to

$$\rho_{\mathtt{GND}} = \frac{\alpha \mathtt{KAM}}{bL} \tag{15}$$

where α is a constant that depends on the type of dislocations, and here is set to 3 [49]. b is the magnitude of the Burgers vector, which is 0.2863 nm for the Al alloy tested here. L is the distance over which the KAM is calculated. As it involves only the 4 nearest neighbours, L is the EBSD acquisition step size 0.9 µm. Figure 16c shows the GND density level estimated by commercial software Aztec calculated from Hough-based indexation results. The resulting GND density of grains with high KAM values is overwhelmingly high, thus not reliable. By filtering the PC values and reducing the number of degrees of freedom to the three Euler angles, the KAM level drops down and the fine structures of the sample become visible. This comparison of crystallographic orientation indexing demonstrates that for regular fast EBSD acquisition, standard EBSD comes with an error of 0.5°, while the proposed IDIC EBSD calibration, with the assumption that PC values are smoothly varying, leads to an error of about $0.1° \approx 1.7 \times 10^{-3}$ rad. This drastic drop of uncertainty allows fine structures to be captured. The calculated GND density field from IDIC EBSD calibration is shown in Figure 16d. It is found that high GND density values at grain boundaries tend to extend toward the core of neighbouring grains. For a slightly deformed

Al sample, the estimated GNDs density of $10^{13} - 10^{14}$ m^{-2} is consistent with previous studies [50]. Figure 16e is an enlargement of the rectangular area in Figure 16d, where small angle grain boundaries(SAGB) are clearly visible. The misorientation angle of the SAGB is marked, and IDIC EBSD calibration is capable to detect SAGB as low as 0.3°, while Hough-based indexation can hardly distinguish SAGB of 2°.

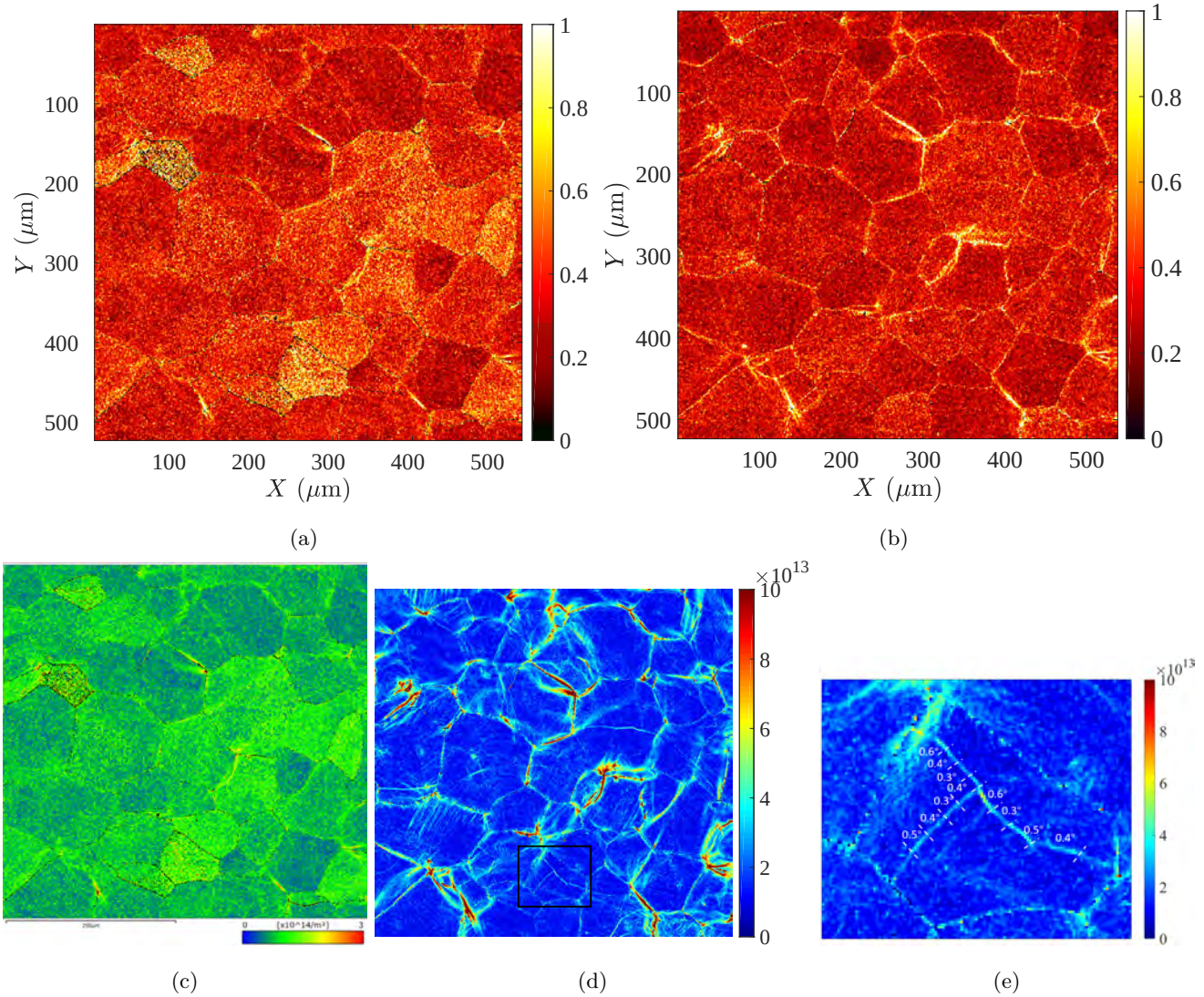

Figure 16: Kernel average misorientation obtained by (a) standard EBSD analyses, (b) IDIC EBSD calibration with 6 parameters of the first pass, (c) GNDs density estimated by commercial Hough-based software Aztec, where a 3×3 kernel size is used. (d) GNDs density estimated by the IDIC EBSD calibration from the 4 closest neighbours. The rectangular region is enlarged in (e). (e) Small angle grain boundaries revealed by IDIC EBSD, with the misorientation marked.

In terms of computation time for 350,000 EBSPs of size 120×160, IDIC EBSD calibration requires about 60 hours on an HP laptop Zbook15 for the first pass, and 40 hours for the second pass with imposed filtered PC values. Although the computation is longer than for the conventional Hough-transformation-based software (3 hours for Aztec), the computation time remains acceptable (and can be potentially reduced, as the present code was not

optimized). In addition, the new full-field projection center information and the high precision of Euler angles estimates make the proposed approach appealing for highly demanding applications.

Table 1: Summary of IDIC EBSD calibration performance on experimental EBSPs of polycrystal Al-Mg alloy
.

Stress state	unstrained	unstrained	5% strain
EBSP size	1200×1600	120×160	120×160
Computation time per EBSP (s)	25	1.7	1.9
Deviation of PC (pixels)	0.38	0.35	0.45
Median KAM with floating PC (degrees)	0.041	0.24	0.31
Median KAM with filtered PC (degrees)	0.035	0.055	0.085

The performance of IDIC EBSD calibration is summarized in Table 1. It is concluded that the proposed calibration procedure was successfully applied to different samples and detectors of various quality. Remap with filtering PC fields can refine Euler angles, and this effect is more significant for smaller EBSPs, which is the case for most EBSD acquisitions. When processing fast and coarse EBSD acquisitions, the IDIC EBSD remapping can reveal fine structures such as GNDs with a better precision.

6 Conclusion

This paper has revisited the main ideas exploited in EBSD indexation. To process diffraction pattern images an Integrated DIC is proposed, that allows one to both determine the crystal orientation but also the Pattern Center from a registration with a direct simulation. Through two virtual tests on simulated EBSPs and two experimental EBSD datasets, (a high definition acquisition, and a fast one) the performance of the algorithm was extensively tested.

The proposed algorithm has the following advantages:

1. Fast convergence. Gradient-based Newton's method is well known for its speed in optimization for smooth cost functions. The mathematical formulation of IDIC proposed in the present paper reduces the number of unknowns to only those that are sought, making the problem much better conditioned than other formulations with extraneous degrees of freedom, and hence more prone to noise. Using the initializations provided by other softwares (`DynamicS`, `Aztec`, etc.), the computation time on HP ZBook15 is about 1 second for a 120×160 pixel detector and 25 seconds for a high definition 1200×1600 pixel one. Such a computation cost (which could be reduced with a more optimized code) though slower than the conventional Hough-transformation software, makes the procedure affordable not only for EBSD calibration at a few points, but also in EBSD indexation of large datasets as shown repeatedly in the present paper.

2. Robustness of calculation. The 6 projection parameters are directly computed by analyzing the whole diffrac-

tion image. This property has been validated on noisy, low-definition EBSPs. Even at grain boundaries where the EBSP consists of several overlapping crystal orientations, different Euler angles can be used as initial values and the smallest residuals can be chosen in the end.

3. The strategy of global correlation reduces the measurement uncertainty. Since the algorithm takes the entire EBSP in the optimization, and weighs each pixel with the inverse variance of residuals, IDIC EBSD calibration is optimal in terms of least sensitivity to white Gaussian noise corrupting diffraction images, and mitigate detector artefacts.

4. Easily tunable. The hereby presented IDIC EBSD algorithm can be easily modified to tailor it to different cases. For example, if the EBSD calibration is successfully conducted (not necessarily by the present method), the pattern center values can be set (*i.e.,* not optimized) and improve the Euler angle precision significantly, as shown in section 5. It is also possible to index 2 independent triplets of Euler angles from overlapped EBSPs, as will be shown in a future work.

5. The residual field of the correlation technique is intrinsically obtained by integrated DIC, while it is not naturally calculated from Hough transformation and dictionary indexing approaches. The residual field is a good indicator of the computation performance. The information contained in the residual maps can be exploited in different ways, such as mitigating the EBSP noise from an optimal formulation of the IDIC cost function.

Our EBSD calibration strategy shows good performance on both high resolution EBSPs and fast rate EBSPs of 120×160 pixel, in the latter one the GNDs and intragranular substructures of as low as 0.3° misorientation can be clearly identified. It also proves better tolerant to rough surface than conventional EBSD indexation methods. Therefore this method shows great potential in the in-situ EBSD experiments for the demanding microstructural studies, such as grain subdivision during deformation.

Last, the proposed algorithm, which is adapted to EBSD calibration, could be extended to several other types of diffraction images (*e.g.,* Kossel, Laue, or TEM diffraction). These techniques derive from the same principles of projection of diffracted beams and, after a simple modification, IDIC-EBSD could be applied to those images as well. Integrated calibration algorithms for Laue and TEM diffraction, with all the above cited advantages, would bring significant benefits to their exploitations.

Acknowledgements

This work is financially supported by the National Natural Science Foundation of China [Nos. 51901132, 51701120]. Dr. Yang Yang from Bruker China is thanked for her assistance in EBSD related Bruker software usages. Dr. Ian Anderson from Oxford Instrument is thanked for providing information about the NordlysMax3 EBSD detector.

References

[1] B. Gaskey, L. Hendl, X. Wang, and M. Seita. Optical characterization of grain orientation in crystalline materials. *Acta Materialia*, 194:558 – 564, 2020.

[2] W.H. Wang, X. Sun, G.D. Köhlhoff, and K. Lücke. Orientation determination by continuous etching patterns in copper and copper alloys. *Textures and Microstructures*, 1995.

[3] D. Jha, S. Singh, R. Al-Bahrani, W. Liao, A. Choudhary, M. De Graef, and A. Agrawal. Extracting grain orientations from EBSD patterns of polycrystalline materials using convolutional neural networks. *Microscopy and Microanalysis*, 24(5):497–502, 2018.

[4] Y. Shen, R. Pokharel, T.J. Nizolek, A. Kumar, and T. Lookman. Convolutional neural network-based method for real-time orientation indexing of measured electron backscatter diffraction patterns. *Acta Materialia*, 170:118 – 131, 2019.

[5] F. Ram, S. Zaefferer, T. Jäpel, and D. Raabe. Error analysis of the crystal orientations and disorientations obtained by the classical electron backscatter diffraction technique. *Journal of Applied Crystallography*, 48(3):797–813, 2015.

[6] L. Li and M. Han. Determining the Bravais lattice using a single electron backscatter diffraction pattern. *Journal of Applied Crystallography*, 48(1):107–115, 2015.

[7] Q. Shi, F. Latourte, F. Hild, and S. Roux. Quaternion correlation for tracking crystal motions. *Measurement Science and Technology*, 27(9):095006, 2016.

[8] A.J. Wilkinson, G. Meaden, and D.J. Dingley. High-resolution elastic strain measurement from electron backscatter diffraction patterns: New levels of sensitivity. *Ultramicroscopy*, 106(4-5):307 – 313, 2006.

[9] A. J. Wilkinson and T. B. Britton. Strains, planes, and EBSD in materials science. *Materials Today*, 15:366–376, 2012.

[10] E. Plancher. *Full-field measurements of elastic and total strains for the determination of the local behaviour in polycrystals*. PhD thesis, Ecole nationale supérieure d'arts et métiers - ENSAM, December 2015.

[11] T. Vermeij and J.P.M. Hoefnagels. A consistent full-field integrated DIC framework for HR-EBSD. *Ultramicroscopy*, 191:44 – 50, 2018.

[12] T.J. Ruggles, G.F. Bomarito, R.L. Qiu, and J.D. Hochhalter. New levels of high angular resolution EBSD performance via inverse compositional Gauss-Newton based digital image correlation. *Ultramicroscopy*, 195:85 – 92, 2018.

[13] Q. Shi, S. Roux, F. Latourte, and F. Hild. Estimation of elastic strain by integrated image correlation on electron diffraction patterns. *Ultramicroscopy*, 199:16–33, 2019.

[14] C. Ernould, B. Beausir, J.-J. Fundenberger, V. Taupin, and E. Bouzy. Global DIC approach guided by a cross-correlation based initial guess for HR-EBSD and on-axis HR-TKD. *Acta Materialia*, 191:131 – 148, 2020.

[15] T. Vermeij, M. De Graef, and J. Hoefnagels. Demonstrating the potential of accurate absolute cross-grain stress and orientation correlation using electron backscatter diffraction. *Scripta Materialia*, 162:266 – 271, 2019.

[16] C. Maurice, R. Fortunier, J. Driver, A. Day, K. Mingard, and G. Meaden. Comments on the paper "Bragg's law diffraction simulations for electron backscatter diffraction analysis" by Josh Kacher, Colin Landon, Brent L. Adams and David Fullwood. 110(7):758 – 759.

[17] G. Nolze, A. Winkelmann, G. Cios, and T. Tokarski. Tetragonality mapping of martensite in a high-carbon steel by ebsd. page 111040.

[18] BLG PRODUCTIONS LTD. Methods, apparatuses and computer programs for crystallography, 10 2012.

[19] D.A. Carpenter, J.L. Pugh, G.D. Richardson, and L.R. Mooney. Determination of pattern centre in EBSD using the moving-screen technique. *Journal of Microscopy*, 227(3):246–247, 2007.

[20] C. Maurice, K. Dzieciol, and R. Fortunier. A method for accurate localisation of EBSD pattern centres. *Ultramicroscopy*, 111(2):140 – 148, 2011.

[21] T.B. Britton, C. Maurice, R. Fortunier, J.H. Driver, A.P. Day, G. Meaden, D.J. Dingley, K. Mingard, and A.J. Wilkinson. Factors affecting the accuracy of high resolution electron backscatter diffraction when using simulated patterns. *Ultramicroscopy*, 110(12):1443 – 1453, 2010.

[22] E.L. Pang, P.M. Larsen, and C.A. Schuh. Global optimization for accurate determination of EBSD pattern centers. *Ultramicroscopy*, 209:112876, 2020.

[23] B.E. Jackson, J.J. Christensen, S. Singh, M. De Graef, D.T. Fullwood, E.R. Homer, and R.H. Wagoner. Performance of dynamically simulated reference patterns for cross-correlation electron backscatter diffraction. *Microscopy and Microanalysis*, 22(4):789–802, 2016.

[24] S. Singh, F. Ram, and M. De Graef. Emsoft: Open source software for electron diffraction/image simulations. *Microscopy and MicroAnalysis*, 23:S1:212–213, 2017.

[25] S. Vespucci, G. Naresh-Kumar, C. Trager-Cowan, K. P. Mingard, D. Maneuski, V. O'Shea, and A. Winkelmann. Diffractive triangulation of radiative point sources. *Applied Physics Letters*, 110(12):124103, 2017.

[26] G. Nolze, M. Jürgens, J. Olbricht, and A. Winkelmann. Improving the precision of orientation measurements from technical materials via EBSD pattern matching. *Acta Materialia*, 159:408 – 415, 2018.

[27] T. Tanaka and A.J. Wilkinson. Pattern matching analysis of electron backscatter diffraction patterns for pattern centre, crystal orientation and absolute elastic strain determination - accuracy and precision assessment. *Ultramicroscopy*, 202:87 – 99, 2019.

[28] T. Friedrich, A. Bochmann, J. Dinger, and S. Teichert. Application of the pattern matching approach for EBSD calibration and orientation mapping, utilising dynamical EBSP simulations. *Ultramicroscopy*, 184:44 – 51, 2018.

[29] A. Winkelmann, B.M. Jablon, V.S. Tong, C. Trager-Cowan, and K.P. Mingard. Improving EBSD precision by orientation refinement with full pattern matching. *Journal of Microscopy*, 277(2):79–92, 2020.

[30] A. Winkelmann, G. Nolze, G. Cios, T.Tokarski, and P. Bała. Refined calibration model for improving the orientation precision of electron backscatter diffraction maps. *Materials*, 13:2816, 06 2020.

[31] B. Wagne, S. Roux, and F. Hild. Spectral approach to displacement evaluation from image analysis. *European Physical Journal: Applied Physics*, 17:247–252, 2002.

[32] G. Besnard, F. Hild, and S. Roux. "Finite-Element" displacement fields analysis from digital images: application to Portevin-Le Chatelier bands. *Experimental Mechanics*, 46:789–803, 2006.

[33] F. Hild and S. Roux. Digital image correlation: from displacement measurement to identification of elastic properties - a review. *Strain*, 42(2):69–80, 2006.

[34] S. Roux and F. Hild. Stress intensity factor measurements from digital image correlation: post-processing and integrated approaches. *International Journal of Fracture*, 140(1):141–157, 2006.

[35] H. Leclerc, J.-N. Périé, S. Roux, and F. Hild. Integrated digital image correlation for the identification of mechanical properties. *MIRAGE 2009, LNCS*, 5496:161–171, 2009.

[36] P. Callahan and M. Graef. Dynamical electron backscatter diffraction patterns. part i: Pattern simulations. *Microscopy and microanalysis*, 19:1–11, 2013.

[37] C. T. Young and J. L. Lytton. Computer generation and identification of kikuchi projections. *Journal of Applied Physics*, 43(4):1408–1417, 1972.

[38] J. Alkorta. Limits of simulation based high resolution EBSD. *Ultramicroscopy*, 131:33 – 38, 2013.

[39] J. Alkorta, M. Marteleur, and P.J. Jacques. Improved simulation based HR-EBSD procedure using image gradient based DIC techniques. *Ultramicroscopy*, 182:17 – 27, 2017.

[40] D. Fullwood, M. Vaudin, C. Daniels, T. Ruggles, and S.I. Wright. Validation of kinematically simulated pattern HR-EBSD for measuring absolute strains and lattice tetragonality. *Materials Characterization*, 107(Supplement C):270 – 277, 2015.

[41] Q. Shi, S. Roux, F. Latourte, F. Hild, D. Loisnard, and N. Brynaert. On the use of SEM correlative tools for in situ mechanical tests. *Ultramicroscopy*, 184(Part A):71 – 87, 2018.

[42] F. Hild and S. Roux. Digital image correlation. In P. Rastogi and E. Hack, editors, *Optical Methods for Solid Mechanics. A Full-Field Approach*, pages 183–228. Wiley-VCH, Weinheim (Germany), 2012.

[43] B. Pan, H. Xie, and Z. Wang. Equivalence of digital image correlation criteria for pattern matching. *Applied Optics*, pages 5501–5509, 2010.

[44] T.B. Britton, J. Jiang, Y. Guo, A. Vilalta-Clemente, D. Wallis, L.N. Hansen, A. Winkelmann, and A.J. Wilkinson. Tutorial: Crystal orientations and EBSD - or which way is up? *Materials Characterization*, 117:113 – 126, 2016.

[45] A. Seret, C. Moussa, M. Bernacki, J. Signorelli, and N. Bozzolo. Estimation of geometrically necessary dislocation density from filtered EBSD data by a local linear adaptation of smoothing splines. *Journal of Applied Crystallography*, 52(3):548–563, 2019.

[46] A. Winkelmann, G. Cios, T. Tokarski, G. Nolze, R. Hielscher, and T. Kozieł. EBSD orientation analysis based on experimental Kikuchi reference patterns. *Acta Materialia*, 188:376 – 385, 2020.

[47] A. Winkelmann. Dynamical effects of anisotropic inelastic scattering in electron backscatter diffraction. *Ultramicroscopy*, 2008.

[48] F. Ram and M. Graef. Energy dependence of the spatial distribution of inelastically scattered electrons in backscatter electron diffraction. 97:134104.

[49] P. Konijnenberg, S. Zaefferer, and D. Raabe. Assessment of geometrically necessary dislocation levels derived by 3D EBSD. *Acta Materialia*, 99:402–414, 2015.

[50] J.F. Derakhshan, M.H. Parsa, and H.R. Jafarian. Microstructure and mechanical properties variations of pure aluminum subjected to one pass of ECAP-Conform process. *Materials Science and Engineering: A*, 747:120 – 129, 2019.